Master's Thesis

Impact of near-inertial waves on a balanced flow

Alexis Riopel,
Department of Atmospheric and Oceanic Sciences,
McGill University, Montréal.

A thesis submitted to McGill University in partial fulfillment of the requirements of the degree of M.Sc. in Atmospheric and Oceanic Sciences.

supervised by
Dr. David Straub

July 2016

Abstract. Near-inertial waves (NIWs), i.e. inertia-gravity waves with a frequency close to f, account for about half of the wave energy in the ocean. Forced mainly by winds, NIWs are ubiquitous in the oceans, superimposed over balanced currents. While NIWs have a strongly depth-dependent structure, the balanced flow is more often vertically uniform over a few hundreds of meters. It is unclear whether NIWs exchange energy with the balanced flow, thus influencing the oceanic circulation. Using a two-layer shallow-water model, we investigate this question. We compare our results with those from Xie & Vanneste (2015), which highlights energy transfers from the balanced flow to NIWs potential energy when the length scale of NIWs reduces. We perform the same numerical experiment they did, where NIWs evolve over a depth-independent vorticity dipole. An important difference with our two-layer model is the interface deformation field between the two layers, and how it affects the kinetic energy budget, sometimes playing an intermediary role in the transfer of energy from the balanced flow to NIWs. We also conduct simulations with a turbulent background flow and a stratification typical of the mid-latitudes. Like Xie & Vanneste (2015), we find that as long as the NIW scale is decreasing because of advection and refraction by the background flow, the wave potential energy is increasing. Moreover, we are able write down a compact expression for the energy transfer from the balanced flow to NIWs. This expression depends on the unbalanced, fast-timescale part of the baroclinic potential vorticity.

L'impact des ondes quasi-inertielles sur le courant en équilibre

Résumé. Les ondes quasi-inertielles (OQI), c'est-à-dire des ondes d'inertie-gravité dont la fréquence diffère peu de f, constituent environ la moitié de l'énergie des vagues dans l'océan. Principalement générées par le vent, les OQI sont omniprésentes dans les océans, superposées à des courants en équilibre. Tandis que les OQI présentent une structure qui varie rapidement le long de l'axe vertical, les courants en équilibre sont plus généralement indépendants de la profondeur. Il n'est pas encore bien compris si les OQI échangent de l'énergie avec les courants en équilibre et influencent la circulation océanique. À l'aide d'un modèle Saint-Venant à deux couches, nous nous penchons sur cette question. Nous comparons nos résultats à ceux de Xie & Vanneste (2015), qui montrent un transfert d'énergie depuis du courant en équilibre vers l'énergie potentielle des OQI lorsque l'échelle spatiale des ondes rapetisse. Nous réalisons la même expérience numérique qu'eux où des OQI évoluent dans un vortex dipolaire. Une différence importante de notre modèle réside dans l'interface entre les deux couches, et comment cette déformation change le bilan d'énergie cinétique, jouant parfois le rôle d'un intermédiaire dans le transfert d'énergie vers les ondes. Nous réalisons aussi des simulations avec un champ turbulent en tant qu'écoulement en équilibre et une stratification typique des latitudes moyennes. Comme Xie & Vanneste (2015), nous constatons que l'énergie potentielle des ondes augmente quand l'échelle spatiale des OQI diminue sous l'effet de l'advection et de la réfraction du courant d'arrière-plan. De plus, nous arrivons à écrire, à l'aide d'une expression compacte, comment l'énergie passe du courant en équilibre aux ondes. Cette expression dépend de la partie à haute fréquence du tourbillonnement potentiel barocline.

Contents

Contents **3**

1 Introduction **5**
1.1 One-layer system . . . 5
1.2 Near-inertial waves . . . 7
1.3 Scale reduction and capture by anti-cyclones . . . 7
1.4 Young and Ben Jelloul model . . . 9
1.5 Energy transfers . . . 10

2 The two-layer shallow-water model **13**
2.1 Barotropic and baroclinic modes . . . 13
2.2 Governing equations . . . 14
2.3 Sets of variables . . . 15
2.4 Decomposition into geostrophic and wave modes . . . 16
2.5 Energy components . . . 17
2.6 Energy equations for the balanced flow . . . 18
Equation for E_t^{ψ} . . . 18
Equation for E_t^{G} . . . 19

3 Numerical results **21**
3.1 Barotropic dipole . . . 21
Initial fields . . . 21
Reference simulation: no background flow . . . 21
First dipole experiment (D1): XV-like . . . 24
Second dipole experiment (D2): stronger dipole . . . 26
Third dipole experiment (D3): "realistic" parameters . . . 27
Time evolution of the balanced flow . . . 30
3.2 Turbulent flows . . . 31
First turbulent experiment (T1): weak stratification . . . 32
Second turbulent experiment (T2): medium stratification . . . 32
Third turbulent experiment (T3): strong stratification . . . 33
Time evolution of the balanced flow . . . 35

4 Discussion and Conclusion **37**

4.1 Dipole experiments: comparison between models 37
Generalised-Lagrangian-mean model 37
Two-layer shallow-water model 37
E^C as an intermediary 38
Breaking of the wave action conservation 39
4.2 Experiment T1: transfer from the background flow to the wave potential energy . 40
4.3 Conclusion 43

Bibliography **45**

Chapter 1

Introduction

Compared with Earth's radius, the ocean is very thin. Covering a basketball with aluminum foil will give the same ratio of thickness over diameter. In this fine layer evolve all currents, from the powerful Agulhas off the tip of Southern Africa to deep convection in Labrador sea. A panoply of waves also propagate into this near two-dimensional water mass.

A major feature of Earth is, of course, that it is rotating. Ocean dynamics are therefore qualitatively different from what one would expect to find in his kitchen sink. A dominant force is, in a geophysical context, the Coriolis force. This acceleration is only felt within the rotating reference frame. When the pressure gradient and the Coriolis are of equal magnitudes and in opposite directions, a geostrophically balanced flow results.

If no force is balancing Coriolis, the fluid will accelerate. However, this acceleration is perpendicular to the motion of the water parcel, and energy is conserved. This kind of circular motion is called an inertial oscillation. After an inertial period, the water parcel has completed a loop and is back to its initial location, if no other force are at play.

Superimposed over geostrophic currents and inertial oscillations are gravity waves. Generally, the restoring force acts strongly, and so the period of those gravity waves is short compared with an inertial period. "Inertia-gravity wave" (IGWs) is a more general name for any wave that is affected by both the referential rotation and gravity. The frequency of these waves is between f, the Coriolis frequency (lower boundary), and N, the buoyancy frequency (upper boundary). In most oceanic conditions, energy is concentrated in the near-inertial band of the spectrum.

1.1 One-layer system

A simple system containing all of the aforementioned physical phenomena is the linearized shallow-water equations. This set of equations, valid for a thin incompressible fluid, goes like this:

$$\boldsymbol{u}_t = -f\hat{\boldsymbol{z}} \times \boldsymbol{u} - g\boldsymbol{\nabla}\eta, \tag{1.1}$$

$$\eta_t = -H\boldsymbol{\nabla} \cdot \boldsymbol{u}, \tag{1.2}$$

The subscript t represents a temporal derivative, $\boldsymbol{u}$ is the velocity vector, η is the surface deformation, f is the Coriolis frequency, $\boldsymbol{\nabla}$ is the horizontal gradient operator, g is the gravity acceleration and H is the layer thickness.

Within this simple model, the basic dynamics of the ocean are present:

$$\text{geostrophic balance} \quad f\hat{\boldsymbol{z}} \times \boldsymbol{u} = -g\boldsymbol{\nabla}\eta, \tag{1.3}$$

$$\text{inertial waves} \quad \eta_{tt} = -f^2\eta, \tag{1.4}$$

$$\text{gravity waves} \quad \eta_{tt} = gH\boldsymbol{\nabla}^2\eta. \tag{1.5}$$

We will now derive Poincaré waves, i.e. IGWs in a one-layer flow. First of all, we take the divergence of $\boldsymbol{u}_t$. We then put it into the mass conservation equation, of which we had previously taken the time derivative:

$$\eta_{tt} = gH\boldsymbol{\nabla}^2\eta - fH\zeta. \tag{1.6}$$

$\zeta = v_x - u_y$ is the relative vorticity (subscripts are here derivatives). We now need a way to express ζ as a function of η in order to close the wave equation. If we take the curl of $\boldsymbol{u}_t$, we find

$$\zeta_t + f\delta = 0, \tag{1.7}$$

where δ is the divergence $u_x + v_y$. Plugging in the conservation equation, we get

$$\zeta_t = \tfrac{f}{H}\eta_t \implies \zeta = \tfrac{f}{H}\eta + \text{constant}. \tag{1.8}$$

The integration constant is zero because far away from all surface deformation, the velocities are uniform and therefore $\zeta = 0$. We now assume that a plane-wave solution $\eta \sim \exp(i\omega t - i\boldsymbol{k}\cdot\boldsymbol{x})$ can satisfy the updated equation (1.6),

$$\eta_{tt} = gH\boldsymbol{\nabla}^2\eta - f^2\eta. \tag{1.9}$$

We then find the Poincaré wave dispersion relation:

$$\omega^2 = f^2 + c^2\kappa^2, \tag{1.10}$$

where $c^2 = gH$ and κ is the norm of the horizontal wavevector.

The two roots of ω corresponds to two eigenvalues, for each wave vector $\boldsymbol{k}$. These two eigenvectors, named W^+ and W^-, in addition to the geostrophic balance, describe completely the flow. The frequency associated with the geostrophic mode, labeled G, is zero, as it does not depend on time. $W^+(\boldsymbol{k})$, $W^-(\boldsymbol{k})$ and $G(\boldsymbol{k})$ form a complete basis for any flow in the context of the linear shallow-water equations. A detailed derivation of this decomposition will be given in section 2.4.

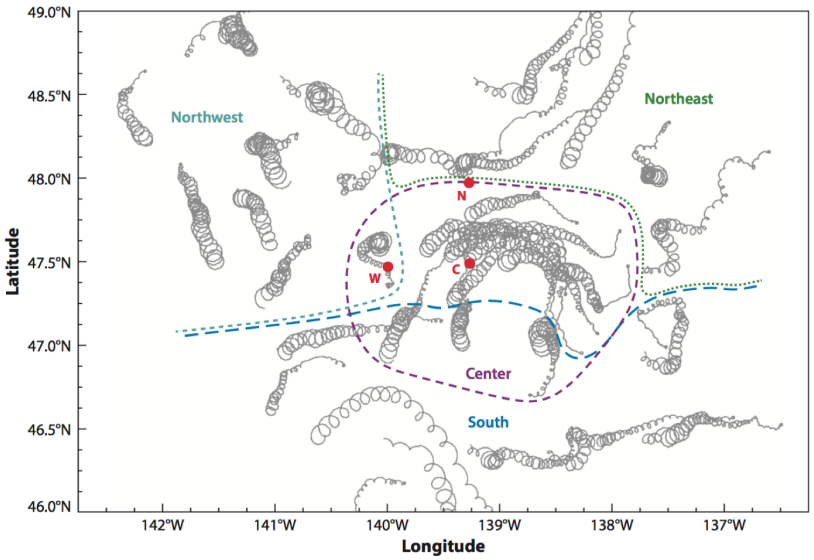

Figure 1: Drifter tracks exhibiting a near-inertial motion. Figure adapted from D'Asaro et al. (1995).

1.2 Near-inertial waves

The focus of this study is near-inertial waves (NIWs). NIWs are characterized, according to Alford et al. (2016), by a frequency between f and $1.2f$ and by a characteristic scale of 10-100 km. Figure 1 shows drifter trajectories in a NIWs field, following the passage a storm. The tracks describe rotational motions, advected over the domain by a slower current. This figure shows with clarity that waves are superposed over the mesoscale oceanic circulation.

According to many observational studies, there is a tendency for energy to pile up in the near-inertial (NI) band of the wave spectrum (e.g. figure 2). A few mechanisms account for the accumulation of energy in the NI band: interactions between geostrophic currents and the bottom topography (Nikurashin and Ferrari, 2010), resonant interactions with tides at specific latitudes (Young et al., 2008), nonlinear interactions between geostrophic currents and NIWs (Gertz and Straub, 2009; Xie and Vanneste, 2015), and most importantly, forcing by wind.

Fluctuations in time and space of the wind forcing on the water surface generate NIWs. Resonance with $f\hat{\boldsymbol{k}} \times \boldsymbol{u}$ in the momentum equation is one reason why NIWs are dominant in the wave spectrum. Many wind events contain energy at the resonant frequency, namely hurricanes, storms and even diurnal breezes near land at 30° latitude. These forcings are usually of large spatial extent, e.g. synoptic scale of O(1000 km), whereas the ocean mesoscale is much smaller with O(30 km).

1.3 Scale reduction and capture by anti-cyclones

Notice that NIWs are forced at large scale, whereas observations show they exist predominantly at smaller scales. There has to be mechanisms that stretch, refract, break apart and globally reduce NIWs scale. The planetary vorticity gradient (β-effect) and the the mesoscale background

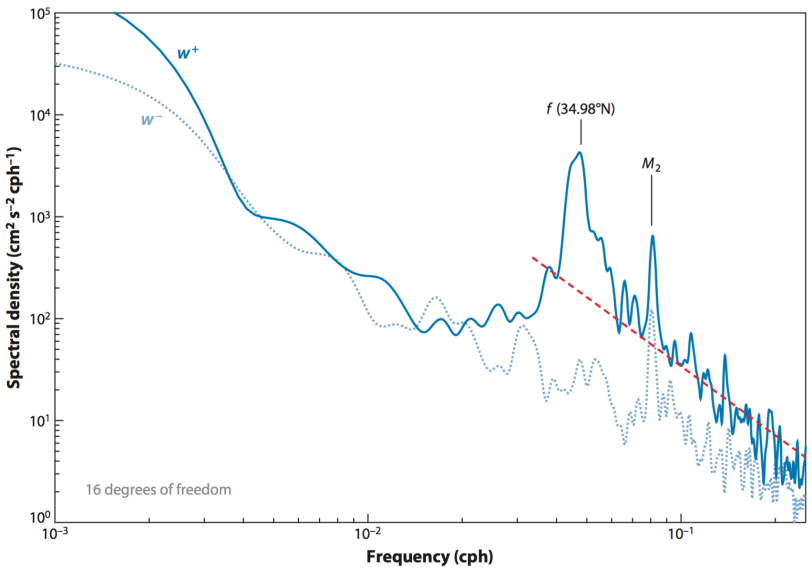

Figure 2: Rotary velocity spectrum at a depth of 261 m. W^+ is the clockwise energy and W^- the counterclockwise energy. WESTPAC1 experiment, figure from Alford et al. (2016).

flow play this role.

The planetary vorticity can be approximated as $f = f_0 + \beta y$. With the consideration of β, the inertial frequency varies with latitude. Suppose that a large synoptic event impinges an uniform velocity to water on a surface spanning a thousand kilometers along the meridional direction. Waves at the southern and northern limits of the domain would oscillate at their local inertial frequencies, which are f_0 and $f_0 + \beta(10^6 \text{ m})$. The phase difference between both locations is then $\beta(10^6 \text{ m})(t - t_0)$. With typical parameters for mid-latitudes ($f_0 = 10^{-4}$ s^{-1} and $\beta = 2 \times 10^{-11}$ m^{-1}s^{-1}), a difference of π in phase is reached after about 2 inertial periods. This phase difference reduces the effective wavelength of the inertial oscillations, because velocities at the northern and southern limits of the domain are now in opposite directions.

The impact of the background flow on the spatial distribution of NIWs has been carefully studied. Following observations by Kunze and Sanford (1984), Kunze (1985) proposed a mechanism using a Wentzel–Kramers–Brillouin (WKB) ray-tracing approach. He postulated an unchanging background current over which are superimposed NIWs. The vorticity of the background flow would add up to the planetary vorticity and make up a new effective inertial frequency $f_{\text{eff}} = f + \frac{1}{2}\zeta$. WKB theory then postulates that each wavelet conserves its characteristic frequency, and so each one would be refracted towards regions of negative vorticity. The explanation is analogous to light propagating in a medium of non-uniform refraction index. NIWs are trapped inside anticyclones and expelled from cyclones. Through this refraction mechanism, NIWs are shrunk to the size of the background vorticity smaller features, and even smaller.

An import caveat of Kunze (1985)'s explanation is that WKB theory requires the spatial variations in the wave phase to be much smaller than its wavelength, and this is not true for the refraction of large scale NIWs by smaller scale features in the background vorticity.

Nonetheless, the theory gives useful intuition as to how the mesoscale field distorts NIWs and brings them to smaller scales.

1.4 Young and Ben Jelloul model

A few years later, Young and Ben Jelloul (1997) (hereafter YBJ) built a new framework to explain how NIWs propagate through a geostrophic flow. Their theory necessitates a clear-cut timescale separation between waves and background flow, but no spatial scale separation is needed. The basic idea is that they average out inertial waves and keep only a slowly-evolving envelope. Like Kunze (1985), they find a refraction term stemming from the mixed wave-background advection $[\boldsymbol{u}\cdot\boldsymbol{\nabla}]\boldsymbol{U}$ of the momentum, where $\boldsymbol{U}$ is the background velocity and $\boldsymbol{u}$ is the wave velocity. Their framework has an energy conservation law that makes impossible any energy transfer between waves and the geostrophic flow.

YBJ's framework has different versions, and we will now get a sense of it using the reduced-gravity shallow-water system presented in Danioux et al. (2015). They start with the shallow-water equations linearized about a barotropic base state $(U, V) \gg (u, v)$. They assume a weak and static background flow (small Ro) and waves oscillating at a frequency close to f_0 (small Burger number). They rewrite the shallow-water system using $(u + iv)$ as a variable and keep only the leading order solution, the small parameter being $\epsilon \sim \mathrm{Ro} \sim \mathrm{Bu}$. After some algebra, they are only left with the slow evolution of NIWs, reading

$$M_t = -\mathsf{J}(\psi, M) + \frac{if_0L_d^2}{2}\nabla^2 M - \frac{i\nabla^2\psi}{2}M, \tag{1.11}$$

$$\text{where } M = (u + iv)\mathrm{e}^{-if_0t}. \tag{1.12}$$

M is the complex wave amplitude, J is the Jacobian, ψ is the barotropic streamfunction and L_d is the relevant deformation radius (see section 2.1). On the right-hand side of equation 1.11, one can recognize three terms acting on NIWs: advection by the background flow, dispersion due to stratification, and refraction by the background vorticity. This last term is responsible for the cascade to smaller scale of the NI field. We will look more closely at its construction.

We will express the background flow using $\boldsymbol{U} = (-\psi_y, \psi_x)$ and the wave field with $\mathscr{U} = u + iv$. Therefore,

$$u = \frac{\mathscr{U} + \mathscr{U}^*}{2}, \quad v = \frac{\mathscr{U} - \mathscr{U}^*}{2i}, \tag{1.13}$$

where the asterisk denotes a complex conjugate. The momentum equation they use is the following:

$$\boldsymbol{u}_t = -f\hat{\boldsymbol{z}}\times\boldsymbol{u} - [\boldsymbol{U}\cdot\boldsymbol{\nabla}]\boldsymbol{u} - [\boldsymbol{u}\cdot\boldsymbol{\nabla}]\boldsymbol{U} - g'\boldsymbol{\nabla}\eta. \tag{1.14}$$

Refraction by the background vorticity, our current focus of interest, is caused by the third term on the right-hand side of the last expression, so we will only keep this term. If we replace $\boldsymbol{U}$ and $\boldsymbol{u}$ by ψ and $\mathscr{U}$, we are left with

$$\mathscr{U}_t = -\frac{i}{2}\mathscr{U}\nabla^2\psi + \mathscr{U}^*\left(\psi_{xy} + \frac{i}{2}\psi_{xx} - \frac{i}{2}\psi_{yy}\right) \tag{1.15}$$

The important thing to notice here is that $\mathscr{U}^*$ is out of phase with the rest of the equation. For example, using $\mathscr{U} = Me^{if_0t}$ and dividing the resulting equation by e^{if_0t}, one finds

$$-if_0M = -\frac{i}{2}M\nabla^2\psi + e^{-2if_0t}M^*\left(\psi_{xy} + \frac{i}{2}\psi_{xx} - \frac{i}{2}\psi_{yy}\right). \tag{1.16}$$

The rightmost part of the equation is off-resonant and this is why it does not appear in Danioux et al. (2015) nor in our equation (1.11). The first term on the right-hand side of the last expression, $-\frac{i}{2}M\nabla^2\psi$, is the refraction term in (1.11).

1.5 Energy transfers

Gertz and Straub (2009) gave a first look at the problem of energy transfer between a depth-independent flow and inertial waves. They used an unstratified model to study how mid-latitude gyres are interacting with three-dimensional modes. It appears that inertial waves provide a sink of energy for the gyres. Energy is extracted from the balanced flow and low wavenumber and then cascades to smaller scales as inertial waves, before getting dissipated by hyperviscosity.

Taylor and Straub (2016) brought the investigation further with a primitive equation simulation of a stratified flow. They force a flow in channel with both high- and low-frequency winds. Fast NIWs exert Reynolds stresses on the slow flow and act as an energy sink. In particular, a term coined "advective sink" in the low-frequency kinetic energy evolution is responsible for the transfers:

$$\chi = -\boldsymbol{U}_{\text{slow}} \cdot ((\boldsymbol{u}\cdot\boldsymbol{\nabla} + w\hat{\boldsymbol{z}}\partial_z)\boldsymbol{u})_{\text{slow}}\,, \tag{1.17}$$

where $\boldsymbol{u}$ and w are the fast horizontal and vertical velocities. A similar term also is found in the potential energy evolution equation. These transfers take place predominantly in the mesoscale.

Xie and Vanneste (2015) (hereafter XV) also let the background flow interact with NIWs in a YBJ-like framework. Within the weak-ζ and weak-stratification regime, they build a coupled model that, when the background velocity is quasi-geostrophic (QG), reduces to the YBJ's wave equation alongside a modified potential vorticity (PV) inversion equation.

Their starting point is a Lagrangian equivalent to the Boussinesq system. They then express that Lagrangian as a function of a mean-flow map, i.e. with coordinates following the background current. They afterwards keep the largest terms, according to an expansion with regards to Ro and Bu. They are then able to compute the equations of motions using Lagrange's equations. Finally, they assume that the background flow is QG, thus allowing some simplification. They end up with a modified PV inversion equation[1]:

$$q_t = -\mathsf{J}(\psi, q), \tag{1.18}$$

$$\text{where } \; q = \nabla^2\psi + \frac{i}{2f_0}\mathsf{J}(M^*, M) + \frac{1}{4f_0}\nabla^2|M|^2. \tag{1.19}$$

[1] In fact, this is the special version of q where a barotropic flow is considered, as in equation (6.5) of XV. This version will be relevant to the numerical problems we will look at.

The time-evolution equation for M is equation 1.11. Notice that quadratic wave terms impact the relation between q and ζ, and in turn, the value of ψ. The model conserves the total energy, as well as the wave action – equal to the wave kinetic energy divided by f_0. The wave action conservation stems from the symmetry of the Lagrangian to the phase of the waves. As long as the wave amplitude and frequency vary slowly in time and space, the Lagrangian does not depend on the phases and Noether's theorem can be used to derive the action conservation law (Salmon, 1998; Goldstein, 1965). Therefore, wave kinetic energy is conserved in the XV framework.

We can easily relate M and q with $\boldsymbol{u}$ and $\boldsymbol{U}$. Therefore, energy components are

$$\text{background kinetic} \quad E^{\psi} = \frac{1}{2}\int |\boldsymbol{\nabla}\psi|^2 \, \mathrm{d}s, \tag{1.20}$$

$$\text{wave kinetic} \quad E^{W}_{\text{kin}} = \frac{1}{2}\int |M|^2 \, \mathrm{d}s = \text{constant}, \tag{1.21}$$

$$\text{wave potential} \quad E^{W}_{\text{pot}} = \frac{1}{4}\int L_d^2 |\boldsymbol{\nabla} M|^2 \, \mathrm{d}s, \tag{1.22}$$

where $\mathrm{d}s$ is a surface element.

Recall that the NIW scale reduces when waves are refracted by a background current. Therefore, $|\boldsymbol{\nabla} M|^2$ will increase as the wave scale reduces and the wave potential energy will go up. Since the total energy is conserved, this new potential energy has to come from somewhere else. Because the wave kinetic energy is fixed, we conclude the new energy is delivered from the balanced flow. XV call that mechanism "stimulated wave generation."

This leads us to the principal question of this thesis: will a model explicitly resolving NIWs exhibit the same energy transfer from the balanced flow to the waves? Because using the full Navier-Stokes equations would be technically difficult, we will take advantage of the thin aspect ratio of NIWs and work with a two-layer shallow-water model. The simplicity of this system will allow us to explain the mechanism with a dynamical description, and not only rely on an energy budget argument. We will explore the regime of XV, at low Ro and low Bu, but will also go further.

The question of energy transfers between waves and a geostrophic current is an important one, with climatic implications. According to reanalysis studies, about half of the wind work exerted on the ocean occurs in the inertial band (Alford, 2003). The mechanism we are looking for in our idealized set-up could give an interesting insight on the more general problem of the energy transfer of high-frequency motion in the ocean to the balanced, slowly-evolving currents.

Chapter 2

The two-layer shallow-water model

2.1 Barotropic and baroclinic modes

The Poincaré waves introduced earlier evolve on a two-dimensional plane. Even though we want to work with a simple model, a one-layer model is not a good tool to study energy transfers between a vertically-uniform background flow and NIWs. The vertical scale of NIWs is about 100-300 meters (Leaman and Sanford, 1975) while the thickness of a typical background current, say the Gulf Stream, is about 1000 m (Stommel, 1958). We will therefore use a model with two layers of equal thickness, for a total depth of 1000 meters in most runs. The two layers are immiscible and of different densities.

If a one-layer model exhibits waves deforming the surface η_1, a two-layer model also allows waves on the interface η_2 between the two layers. Following Gill (1982), we can describe the flow with two independent vertical modes, called the barotropic (sum of the two layers) and baroclinic (difference of the two layers) modes. Waves traveling on each of these modes have their specific phase speed c_i:

$$c_0 = \sqrt{gH} \simeq 100\text{m/s} \qquad \text{for the barotropic mode,} \tag{2.1}$$

$$c_1 = \sqrt{g'H_e} \simeq 3\text{m/s} \qquad \text{for the baroclinic mode,} \tag{2.2}$$

$$\text{where } g' = g\Delta\rho/\rho_0 \qquad \text{is the reduced gravity} \tag{2.3}$$

$$\text{and } H_e = H_1H_2/H \qquad \text{is the equivalent height.} \tag{2.4}$$

We used $H = 1000$ m and $\Delta\rho/\rho_0 \sim 0.003$, a typical value in the ocean according to Gill (1982). Not only would the barotropic waves cause a computational problem because of their high speed, but also their impact on the dynamics is thought to be small. Because deformation of the surface is small when the barotropic flow features are smaller than the barotropic deformation radius ($\simeq 1000$ km), we can apply the "rigid-lid approximation" on η_1 and ignore the barotropic gravity waves.

From now on, c will only refer to the baroclinic phase velocity. If fact, we will mostly talk in terms of the deformation radius L_d, defined as

$$L_d^2 \equiv \frac{g'H_e}{f_0^2} = \frac{c^2}{f_0^2}. \tag{2.5}$$

The dispersion relation (1.10) is still valid for baroclinic Poincaré waves, with H_e and g' instead of H and g.

$$\omega^2 = f^2 + c^2\kappa^2 = f^2 + g'H_e\kappa^2 = f^2(1 + L_d^2\kappa^2). \tag{2.6}$$

For NIWs, frequency ω is close to f. This means that NIWs are associated with large-scale motion compared to the deformation radius ($\kappa^{-2} \gg L_d^2$).

2.2 Governing equations

As a framework, we will use the two-layer shallow-water equations, with a rigid lid on the top layer:

$$\boldsymbol{u}_{1t} = -f\hat{\boldsymbol{z}} \times \boldsymbol{u}_1 - [\boldsymbol{u}_1 \cdot \boldsymbol{\nabla}]\boldsymbol{u}_1 - \tfrac{1}{\rho}\boldsymbol{\nabla}p_{\text{sfc}}, \tag{2.7}$$

$$\boldsymbol{u}_{2t} = -f\hat{\boldsymbol{z}} \times \boldsymbol{u}_2 - [\boldsymbol{u}_2 \cdot \boldsymbol{\nabla}]\boldsymbol{u}_2 - \tfrac{1}{\rho}\boldsymbol{\nabla}p_{\text{sfc}} - g'\boldsymbol{\nabla}\eta, \tag{2.8}$$

$$\eta_t = -\boldsymbol{u}_2 \cdot \boldsymbol{\nabla}\eta - h_2\boldsymbol{\nabla} \cdot \boldsymbol{u}_2, \tag{2.9}$$

where $\boldsymbol{u}_i$ is the velocity in the ith layer, f is the Coriolis frequency, p_{sfc} is the pressure at the surface, η is the interface deformation and h_i is the ith layer thickness. Subscripts t, x and y designate partial derivatives throughout the thesis. Also, $\boldsymbol{\nabla}$ is the two-dimensional gradient operator and $\boldsymbol{\nabla}\cdot$ is the two-dimensional divergence operator.

We define our baroclinic and barotropic velocities as follows:

$$\boldsymbol{u} \equiv \tfrac{1}{2}(\boldsymbol{u}_2 - \boldsymbol{u}_1), \tag{2.10}$$

$$\boldsymbol{U} \equiv \tfrac{1}{2}(\boldsymbol{u}_2 + \boldsymbol{u}_1). \tag{2.11}$$

We can rewrite the equation system (2.7-2.9) with variables $\boldsymbol{u}$ and $\boldsymbol{U}$.

$$\boldsymbol{u}_t = -f\hat{\boldsymbol{z}} \times \boldsymbol{u} - [\boldsymbol{U} \cdot \boldsymbol{\nabla}]\boldsymbol{u} - [\boldsymbol{u} \cdot \boldsymbol{\nabla}]\boldsymbol{U} - \tfrac{g'}{2}\boldsymbol{\nabla}\eta, \tag{2.12}$$

$$\boldsymbol{U}_t = -f\hat{\boldsymbol{z}} \times \boldsymbol{U} - [\boldsymbol{U} \cdot \boldsymbol{\nabla}]\boldsymbol{U} - [\boldsymbol{u} \cdot \boldsymbol{\nabla}]\boldsymbol{u} - \tfrac{1}{\rho}\boldsymbol{\nabla}p_{\text{sfc}} - \tfrac{g'}{2}\boldsymbol{\nabla}\eta, \tag{2.13}$$

$$\eta_t = -\left(\tfrac{H}{2} + \eta\right)\boldsymbol{\nabla} \cdot (\boldsymbol{u} + \boldsymbol{U}) - (\boldsymbol{u} + \boldsymbol{U}) \cdot \boldsymbol{\nabla}\eta. \tag{2.14}$$

The shallow-water system can also be expressed in a Bernoulli-vorticity form, reading

$$\boldsymbol{u}_{1t} = -(f + \zeta_1)\hat{\boldsymbol{z}} \times \boldsymbol{u}_1 - \boldsymbol{\nabla}B_1 - \tfrac{1}{\rho}\boldsymbol{\nabla}p_{\text{sfc}}, \tag{2.15}$$

$$\boldsymbol{u}_{2t} = -(f + \zeta_2)\hat{\boldsymbol{z}} \times \boldsymbol{u}_2 - \boldsymbol{\nabla}B_2 - \tfrac{1}{\rho}\boldsymbol{\nabla}p_{\text{sfc}} - g'\boldsymbol{\nabla}\eta, \tag{2.16}$$

where $B_i = \frac{1}{2}(u_i^2 + v_i^2)$. We can also combine these equations and find the governing equations for $\boldsymbol{u}$ and $\boldsymbol{U}$.

$$\boldsymbol{u}_t = -(f + \zeta)\hat{\boldsymbol{z}} \times \boldsymbol{u} - \zeta_{\text{bc}}\hat{\boldsymbol{z}} \times \boldsymbol{U} - \tfrac{1}{2}\boldsymbol{\nabla}\left(2\boldsymbol{u} \cdot \boldsymbol{U} + g'\eta\right), \tag{2.17}$$

$$\boldsymbol{U}_t = -(f + \zeta)\hat{\boldsymbol{z}} \times \boldsymbol{U} - \zeta_{\text{bc}}\hat{\boldsymbol{z}} \times \boldsymbol{u} - \tfrac{1}{2}\boldsymbol{\nabla}\left(|\boldsymbol{u}|^2 + |\boldsymbol{U}|^2 + \tfrac{1}{\rho}p_{\text{sfc}} + g'\eta\right), \tag{2.18}$$

where $\zeta \equiv \frac{1}{2}(\zeta_1 + \zeta_2)$ and $\zeta_{\text{bc}} \equiv \frac{1}{2}(\zeta_2 - \zeta_1)$. The equation for η is, as before, (2.14).

2.3 Sets of variables

Different sets of variables can be chosen to describe the flow evolution. In the previous section, we have written the governing equation as functions of the barotropic (U, V) and baroclinic (u, v) velocities. This leads to the basis

$$u, v, \eta, U, V. \tag{2.19}$$

The two-layer shallow-water model, with this choice of variables, features an important difference compared to the QG framework, where the barotropic velocities are divergenceless. Here, U and V have a small divergent component, resulting from the deformation of the interface. To see why, one can look at the vertically-averaged velocity, that goes like

$$\overline{\boldsymbol{U}} \equiv \tfrac{1}{H} \sum_i h_i \boldsymbol{u}_i, \tag{2.20}$$

$$= \left(\tfrac{1}{2} - \tilde{\eta}\right) \boldsymbol{u}_1 + \left(\tfrac{1}{2} + \tilde{\eta}\right) \boldsymbol{u}_2, \tag{2.21}$$

$$= \boldsymbol{U} + 2\tilde{\eta}\boldsymbol{u}, \tag{2.22}$$

where $\tilde{\eta} = \eta/H$. By definition, $\boldsymbol{\nabla} \cdot \overline{\boldsymbol{U}}$ is zero. No mass can enter nor leave a location in the domain because the top and bottom boundaries are rigid. One can then conclude that

$$\boldsymbol{\nabla} \cdot \boldsymbol{U} = \boldsymbol{\nabla} \cdot (-2\tilde{\eta}\boldsymbol{u}) \tag{2.23}$$

i.e. the divergence of $\boldsymbol{U}$ is not zero in general.

For algorithmic reasons, we will use $\overline{\boldsymbol{U}}$ in the numerical solver of our model. For analysis purposes, we will use $\boldsymbol{U}$ because it relates more easily with Gill (1982) vertical modes decomposition and with a QG description of the flow. We know that $\boldsymbol{U}$ has a non-zero divergence, but we also know it is small as long as $\eta \ll H$, according to (2.23). We will describe the divergenceless part of the flow with the streamfunction ψ and the irrotational part with the potential ϕ.

$$U = -\psi_y + \phi_x \tag{2.24}$$

$$V = +\psi_x + \phi_y \tag{2.25}$$

We also want to write down our baroclinic variables in another basis. We will make use of the modes obtained with the wave- and geostrophic-mode decomposition performed in section 2.4. u, v and η can be written as two wave modes W^+ and W^- and a baroclinic geostrophic mode labeled G. These three modes form a complete basis for the baroclinic flow. We are left with the variables we will work with:

$$W, G, \psi, \phi, \tag{2.26}$$

where the two wave modes were combined together. Take note that ψ and ϕ are dependent on W and G because equation (2.22) can be rearranged as

$$\overline{\boldsymbol{U}} - 2(\tilde{\eta}_G \boldsymbol{u}_G + \tilde{\eta}_G \boldsymbol{u}_W + \tilde{\eta}_W \boldsymbol{u}_G + \tilde{\eta}_W \boldsymbol{u}_W) = \boldsymbol{\nabla}_\perp \psi + \boldsymbol{\nabla}\phi \tag{2.27}$$

where $\boldsymbol{\nabla}_\perp = -\partial_y \hat{\boldsymbol{x}} + \partial_x \hat{\boldsymbol{y}}$.

2.4 Decomposition into geostrophic and wave modes

In Fourier space, the baroclinic flow can be described by a set of two inertia-gravity waves and a geostrophic mode at each wavenumber $\boldsymbol{k} = (k, l)$. This linear decomposition is useful when trying to isolate NIWs from the rest of the flow. Recall that we already briefly described this decomposition in section 1.1. We will now follow the method of Salmon (1998) in order to actually perform the change of basis. Salmon (1998) developed his decomposition using a single-layer linearized shallow-water model like (1.1-1.2). Even if the waves we study evolve as a baroclinic mode within a two-layer model, the algebra stays the same.

Before switching to Fourier space, we will combine all baroclinic variables in a single convenient complex variable Θ

$$\Theta(\boldsymbol{x}, t) = \begin{bmatrix} \sqrt{H}u(\boldsymbol{x}, t) \\ \sqrt{H}v(\boldsymbol{x}, t) \\ \sqrt{g'}\eta(\boldsymbol{x}, t) \end{bmatrix}. \tag{2.28}$$

In Fourier space, (1.1-1.2) imply

$$i\frac{\mathrm{d}\Theta(\boldsymbol{k})}{\mathrm{d}t} = \begin{bmatrix} 0 & if_0 & kc \\ -if_0 & 0 & lc \\ kc & lc & 0 \end{bmatrix} \Theta(\boldsymbol{k}). \tag{2.29}$$

Notice the striking similarity with Schrödinger's equation. Now, like any quantum physicist would do, we will compute the eigenvectors and eigenvalues of the above equation. We get

$$\Theta_1(\boldsymbol{k}) \sim \begin{bmatrix} -ilc \\ +ikc \\ f_0 \end{bmatrix} \qquad \text{Geostrophic balance} \tag{2.30}$$

$$\Theta_{2,3}(\boldsymbol{k}) \sim \begin{bmatrix} \pm\omega k + if_0 l \\ \pm\omega l - if_0 k \\ c(k^2 + l^2) \end{bmatrix} \qquad \text{Inertia-gravity waves (when } \kappa^2 \neq 0) \tag{2.31}$$

$$\Theta_{2,3}(\boldsymbol{k}) \sim \begin{bmatrix} 1 \\ \mp i \\ 0 \end{bmatrix} \qquad \text{Inertia-gravity waves (when } \kappa^2 = 0) \tag{2.32}$$

where ω is the positive root of $(f_0^2 + c^2\kappa^2)^{1/2}$. These eigenfunctions are normalized such that $\sum_i |\Theta_i|^2 = 1$ for all $\boldsymbol{k}$. When we project the eigenvectors on the actual flow at time t_0, we end up with coefficients $C_i(\boldsymbol{k}, t_0)$. With these coefficients, it is easy to reconstruct the flow,

$$\Theta(\boldsymbol{x}, t) = \Sigma_i C_i(\boldsymbol{k}, t_0)\Theta_i(\boldsymbol{k})\mathrm{e}^{-i\Omega_i(t-t_0)}, \tag{2.33}$$

where Ω_1=0 and $\Omega_{2,3} = \pm\omega$.

For our purposes, this decomposition will be useful to separate wave and geostrophic modes of the baroclinic flow outputted by our two-layer nonlinear shallow-water system. We will therefore perform the decomposition at each time t and only make use of the instantaneous

result. We will use $c^2 = g'H_e$. We will be able to find the energy energy associated with each mode:

$$E_i(t) = \frac{1}{2Hn_xn_y} \iint C_i^*(\boldsymbol{k}, t) C_i(\boldsymbol{k}, t)\, \mathrm{d}\boldsymbol{k}. \tag{2.34}$$

If we want, for example, to consider only the potential energy, represented by the third element in the made-up vector $\Theta_i = [\alpha_i; \beta_i; \gamma_i]$, we should weight our sum by the squared norm of γ

$$E_i^{\mathrm{pot}}(t) = \frac{1}{2Hn_xn_y} \iint C_i^*(\boldsymbol{k}, t) C_i(\boldsymbol{k}, t) \gamma_i^*(\boldsymbol{k}) \gamma_i(\boldsymbol{k})\, \mathrm{d}\boldsymbol{k}. \tag{2.35}$$

2.5 Energy components

We are interested in the energy budget within the basis U, V, u, v, η. Notice that because of the interface deformation field, a cross-term exists between the barotropic (bt) and baroclinic (bc) modes in the energy budget. We call it the "cubic" term, E^C. All of the energy budget components are written down below.

$$\text{total} \quad E^T = \frac{1}{2} \iint \left[\left(\frac{1}{2} - \frac{\eta}{H} \right) |\boldsymbol{u}_1|^2 + \left(\frac{1}{2} + \frac{\eta}{H} \right) |\boldsymbol{u}_2|^2 + \frac{g'}{H} \eta^2 \right] \mathrm{d}\boldsymbol{x} \tag{2.36}$$

$$\text{barotropic} \quad E^B = \frac{1}{2} \iint |\boldsymbol{U}|^2\, \mathrm{d}\boldsymbol{x} \tag{2.37}$$

$$\text{bc kinetic} \quad E^K = \frac{1}{2} \iint |\boldsymbol{u}|^2\, \mathrm{d}\boldsymbol{x} \tag{2.38}$$

$$\text{bc potential} \quad E^P = \frac{1}{2} \iint \frac{g'}{H} \eta^2\, \mathrm{d}\boldsymbol{x} \tag{2.39}$$

$$\text{cubic} \quad E^C = 2 \iint \frac{\eta}{H} \boldsymbol{U} \cdot \boldsymbol{u}\, \mathrm{d}\boldsymbol{x} \tag{2.40}$$

We can also separate the barotropic energy into its divergenceless and irrotational parts. Once again, this separation is not orthogonal and yields some "barotropic cross-terms", E^X.

$$\text{bt divergenceless} \quad E^\psi = -\frac{1}{2} \iint \psi \nabla^2 \psi\, \mathrm{d}\boldsymbol{x} \tag{2.41}$$

$$\text{bt irrotational} \quad E^\phi = -\frac{1}{2} \iint \phi \nabla^2 \phi\, \mathrm{d}\boldsymbol{x} \tag{2.42}$$

$$\text{bt cross-terms} \quad E^X = +\frac{1}{2} \iint (2\phi_y \psi_x - 2\phi_x \psi_y)\, \mathrm{d}\boldsymbol{x} \tag{2.43}$$

Finally, the baroclinic energy can be divided between W and G.

$$\text{bc waves} \quad E^W = \frac{1}{2} \iint \left(|\boldsymbol{u}_W|^2 + \frac{g'}{H} \eta_W^2 \right) \mathrm{d}\boldsymbol{x} \tag{2.44}$$

$$\text{bc geostrophic} \quad E^G = \frac{1}{2} \iint \left(|\boldsymbol{u}_G|^2 + \frac{g'}{H} \eta_G^2 \right) \mathrm{d}\boldsymbol{x} \tag{2.45}$$

Note that we could also use (2.34) for E^W and E^G, and it would give the same results.

2.6 Energy equations for the balanced flow

It is of great interest to understand how each term in the energy budget evolves. The balanced modes, i.e. ψ and G, are especially important. Those components of the energy budget are thought to evolve slowly in time. Using the governing equations, we can detail how the different modes are forcing on E^ψ and E^G. A transfer between waves and the balanced flow should be visible amongst the terms of the energy equation. This could give us intuition on the physical mechanism behind the energy transfer.

Equation for E_t^ψ

We will begin with the time-evolution of the barotropic divergenceless energy, E^ψ. From (2.41), we can write E_t^ψ like

$$E_t^\psi = -\iint \zeta_t \psi \, \mathrm{d}\boldsymbol{x}. \tag{2.46}$$

ζ_t is specified by the governing equations of our system and is made up of different parts. Bear in mind that the barotropic vorticity ζ is always equal to $\nabla^2\psi$, because the curl of $\boldsymbol{U}_\phi$ is zero. We will label each of the forcing term with superscripts on the left-hand side of E_t. For example, ${}^{WW}E_t^\psi$ would represent the impact of quadratic wave terms on the barotropic divergenceless energy.

Before splitting E_t^ψ into various components, we have to recall the governing equation for $\boldsymbol{U}$ in Bernoulli-vorticity form:

$$\boldsymbol{U}_t = -(f+\zeta)\hat{\boldsymbol{z}}\times\boldsymbol{U} - \zeta_{\mathrm{bc}}\hat{\boldsymbol{z}}\times\boldsymbol{u} - \tfrac{1}{2}\boldsymbol{\nabla}\left(|\boldsymbol{u}|^2 + |\boldsymbol{U}|^2 + \tfrac{1}{\rho}p_{\mathrm{sfc}} + g'\eta\right). \tag{2.47}$$

We will take the curl of this momentum equation and insert it in (2.46).

$$\zeta_t = \hat{\boldsymbol{z}}\cdot\left(\boldsymbol{\nabla}\times\left[-(f+\zeta)\hat{\boldsymbol{z}}\times\boldsymbol{U} - \zeta_{\mathrm{bc}}\hat{\boldsymbol{z}}\times\boldsymbol{u} - \boldsymbol{\nabla}(\ldots)\right]\right) \tag{2.48}$$

The divergence in $\boldsymbol{U}_t$ vanishes when we take the curl. With the use of a vectorial identity, we rewrite ζ_t as

$$\zeta_t = \boldsymbol{\nabla}\cdot\left[-(f+\zeta)\boldsymbol{U} - \zeta_{\mathrm{bc}}\boldsymbol{u}\right]. \tag{2.49}$$

We will separate U into its divergenceless and irrotational parts: $\boldsymbol{U} = \boldsymbol{\nabla}_\perp\psi + \boldsymbol{\nabla}\phi = \boldsymbol{U}_\psi + \boldsymbol{U}_\phi$. We then find

$$\begin{aligned}
\zeta_t &= \boldsymbol{\nabla}\cdot\left[-(f+\zeta)\boldsymbol{U}_\psi - (f+\zeta)\boldsymbol{U}_\phi - \zeta_{\mathrm{bc}}\boldsymbol{u}\right] && (2.50)\\
&= -(f+\zeta)\boldsymbol{\nabla}\cdot\boldsymbol{U}_\psi - \boldsymbol{U}_\psi\cdot\boldsymbol{\nabla}(f+\zeta) + \boldsymbol{\nabla}\cdot\left[-(f+\zeta)\boldsymbol{U}_\phi - \zeta_{\mathrm{bc}}\boldsymbol{u}\right] && (2.51)\\
&= -\boldsymbol{U}_\psi\cdot\boldsymbol{\nabla}\zeta + \boldsymbol{\nabla}\cdot\left[-(f+\zeta)\boldsymbol{U}_\phi - \zeta_{\mathrm{bc}}\boldsymbol{u}\right], && (2.52)
\end{aligned}$$

where we made use of the fact that $\boldsymbol{\nabla}\cdot\boldsymbol{U}_\psi = 0$. The first term on the right-hand side of (2.52) is the self-advection of the divergenceless barotropic flow. This term should not impact the

energy budget. Actually, a simple integration by part on the whole domain proves it is zero:

$$\iint (\boldsymbol{U}_\psi \cdot \boldsymbol{\nabla}\zeta)\psi \,\mathrm{d}\boldsymbol{x} = \iint (\boldsymbol{\nabla}_\perp \psi \cdot \boldsymbol{\nabla}\zeta)\psi \,\mathrm{d}\boldsymbol{x} \tag{2.53}$$

$$= \iint \boldsymbol{\nabla} \cdot (\zeta \boldsymbol{\nabla}_\perp \psi)\psi \,\mathrm{d}\boldsymbol{x} \tag{2.54}$$

$$= \iint \left[\boldsymbol{\nabla} \cdot (\psi\zeta\boldsymbol{\nabla}_\perp\psi) - \zeta\boldsymbol{\nabla}\psi \cdot \boldsymbol{\nabla}_\perp\psi\right] \mathrm{d}\boldsymbol{x} \tag{2.55}$$

$$= 0, \tag{2.56}$$

because $\boldsymbol{\nabla}\psi \cdot \boldsymbol{\nabla}_\perp\psi = 0$. We work on a doubly periodic domain, so the integral of a divergence on the whole domain is zero. We are now left with a quite compact expression for E_t^ψ:

$$E_t^\psi = -\iint \boldsymbol{\nabla} \cdot \left[-(f+\zeta)\boldsymbol{U}_\phi - \zeta_{\mathrm{bc}}\boldsymbol{u}\right] \psi \,\mathrm{d}\boldsymbol{x}. \tag{2.57}$$

We can break it up to show explicitly which modes contribute to E_t^ψ. We will separate the baroclinic variables into $\boldsymbol{u} = \boldsymbol{u}_W + \boldsymbol{u}_G$, $\eta = \eta_W + \eta_G$ and $\zeta_{\mathrm{bc}} = \zeta_W + \zeta_G$. All of the non-zero terms of the energy equation for E^ψ are listed below.

All non-zero contributions to E_t^ψ

$$^{WW}E_t^\psi = \iint \boldsymbol{\nabla} \cdot (\zeta_W \boldsymbol{u}_W)\psi \,\mathrm{d}\boldsymbol{x} \tag{2.58}$$

$$^{GG}E_t^\psi = \iint \boldsymbol{\nabla} \cdot (\zeta_G \boldsymbol{u}_G)\psi \,\mathrm{d}\boldsymbol{x} \tag{2.59}$$

$$^{WG}E_t^\psi = \iint \boldsymbol{\nabla} \cdot (\zeta_G \boldsymbol{u}_W + \zeta_W \boldsymbol{u}_G)\psi \,\mathrm{d}\boldsymbol{x} \tag{2.60}$$

$$^{\phi}E_t^\psi = \iint \boldsymbol{\nabla} \cdot (f\boldsymbol{U}_\phi)\psi \,\mathrm{d}\boldsymbol{x} \tag{2.61}$$

$$^{\phi\psi}E_t^\psi = \iint \boldsymbol{\nabla} \cdot (\zeta\boldsymbol{U}_\phi)\psi \,\mathrm{d}\boldsymbol{x} \tag{2.62}$$

Equation for E_t^G

Next, we consider the different energy contributions to the baroclinic geostrophic energy. From (2.45), we know that

$$E_t^G = \iint \left(\boldsymbol{u}_G \cdot \boldsymbol{u}_t + \tfrac{g'}{H}\eta_G\eta_t\right) \mathrm{d}\boldsymbol{x} \tag{2.63}$$

Recall the governing equation (2.12) for $\boldsymbol{u}$ in the regular form, as well as governing equation (2.14) for η:

$$\boldsymbol{u}_t = -f\hat{\boldsymbol{z}} \times \boldsymbol{u} - [\boldsymbol{U} \cdot \boldsymbol{\nabla}]\boldsymbol{u} - [\boldsymbol{u} \cdot \boldsymbol{\nabla}]\boldsymbol{U} - \tfrac{g'}{2}\boldsymbol{\nabla}\eta, \tag{2.64}$$

$$\eta_t = -\boldsymbol{\nabla} \cdot \left[\left(\tfrac{H}{2} + \eta\right)(\boldsymbol{u} + \boldsymbol{U})\right]. \tag{2.65}$$

There are very few simplifications that can be done in E_t^G, apart from making use of $\boldsymbol{\nabla} \cdot \boldsymbol{u}_G = 0$ and $\boldsymbol{u}_G \cdot \boldsymbol{\nabla}\eta_G = 0$ (the baroclinic geostrophic flow is divergenceless and along the interface deformation field gradient). We then deduce that

$$
\begin{aligned}
{}^{GG}E_t^G &= -\iint \left(\boldsymbol{u}_G \cdot \left(f\hat{\boldsymbol{z}} \times \boldsymbol{u}_G + \tfrac{g'}{2}\boldsymbol{\nabla}\eta_G \right) + \tfrac{g'}{H}\eta_G \boldsymbol{\nabla} \cdot \left[\boldsymbol{u}_G \left(\tfrac{H}{2} + \eta_G \right) \right] \right) \mathrm{d}\boldsymbol{x} && (2.66)\\
&= 0. && (2.67)
\end{aligned}
$$

This last results holds only for our set-up where the two layers are of equal thicknesses. The other contributions to E_t^G are obtained in a straightforward way by inserting (2.64) and (2.65) in (2.63). They are listed below.

All non-zero contributions to E_t^G

$$
\begin{aligned}
{}^{WW}E_t^G &= -\iint \left(\boldsymbol{u}_G \cdot \left(f\hat{\boldsymbol{z}} \times \boldsymbol{u}_W + \tfrac{g'}{2}\boldsymbol{\nabla}\eta_W \right) + \tfrac{g'}{H}\eta_G \boldsymbol{\nabla} \cdot \left[\boldsymbol{u}_W \left(\tfrac{H}{2} + \eta_W \right) \right] \right) \mathrm{d}\boldsymbol{x} && (2.68)\\
{}^{WG}E_t^G &= -\iint \tfrac{g'}{H}\eta_G \boldsymbol{\nabla} \cdot \left[\boldsymbol{u}_G \eta_W + \boldsymbol{u}_W \eta_G \right] \mathrm{d}\boldsymbol{x} && (2.69)\\
{}^{\phi}E_t^G &= -\iint \tfrac{g'}{2}\eta_G \boldsymbol{\nabla} \cdot \boldsymbol{U}_\phi \, \mathrm{d}\boldsymbol{x} && (2.70)\\
{}^{\psi G}E_t^G &= -\iint \boldsymbol{u}_G \cdot \left([\boldsymbol{U}_\psi \cdot \boldsymbol{\nabla}]\boldsymbol{u}_G + [\boldsymbol{u}_G \cdot \boldsymbol{\nabla}]\boldsymbol{U}_\psi \right) \mathrm{d}\boldsymbol{x} && (2.71)\\
{}^{\phi G}E_t^G &= -\iint \left(\boldsymbol{u}_G \cdot \left([\boldsymbol{U}_\phi \cdot \boldsymbol{\nabla}]\boldsymbol{u}_G + [\boldsymbol{u}_G \cdot \boldsymbol{\nabla}]\boldsymbol{U}_\phi \right) + \tfrac{g'}{H}\eta_G^2 \boldsymbol{\nabla} \cdot \boldsymbol{U}_\phi \right) \mathrm{d}\boldsymbol{x} && (2.72)\\
{}^{\psi W}E_t^G &= -\iint \left(\boldsymbol{u}_G \cdot \left([\boldsymbol{U}_\psi \cdot \boldsymbol{\nabla}]\boldsymbol{u}_W + [\boldsymbol{u}_W \cdot \boldsymbol{\nabla}]\boldsymbol{U}_\psi \right) + \tfrac{g'}{H}\eta_G \boldsymbol{U}_\psi \cdot \boldsymbol{\nabla}\eta_W \right) \mathrm{d}\boldsymbol{x} && (2.73)\\
{}^{\phi W}E_t^G &= -\iint \left(\boldsymbol{u}_G \cdot \left([\boldsymbol{U}_\phi \cdot \boldsymbol{\nabla}]\boldsymbol{u}_W + [\boldsymbol{u}_W \cdot \boldsymbol{\nabla}]\boldsymbol{U}_\phi \right) + \tfrac{g'}{H}\eta_G \boldsymbol{\nabla} \cdot \left(\eta_W \boldsymbol{U}_\phi \right) \right) \mathrm{d}\boldsymbol{x} && (2.74)
\end{aligned}
$$

Chapter 3

Numerical results

3.1 Barotropic dipole

Initial fields

XV performed a numerical experiment highlighting their "stimulated wave generation" mechanism. They use a northward-propagating dipole as a balanced flow. It consists of two side-by-side vortices turning in opposite directions and translating in a straight line at constant speed. We will conduct simulations with the same geometrical set-up as theirs, shown in figure 3, and we will vary a few parameters (dipole size, dipole velocity, L_d, etc). Initial conditions for the dipole fit the following vorticity, in polar coordinates:

$$\zeta(r,\theta) = \begin{cases} \frac{2\kappa_0 U_0}{\mathrm{J}_0(\kappa_0 r_{\mathrm{dip}})} \mathrm{J}_1(\kappa_0 r)\sin\theta & \text{if } r < r_{\mathrm{dip}}, \\ 0 & \text{otherwise.} \end{cases} \tag{3.1}$$

Here, U_0 is the speed of the dipole, r_{dip} is its spatial scale, J_n are the Bessel function of the first kind of order n, and κ_0 satisfies $\mathrm{J}_1(\kappa_0 r_{\mathrm{dip}}) = 0$. We also choose the coordinate system to be initially centered on $(x, y) = (0, y_{\mathrm{dip}})$. Notice that the initial barotropic flow is divergenceless.

Along its way, the dipole encounters a NIW jet. This jet is characterized by a Gaussian function. η is chosen to satisfy $\zeta = 2f\tilde{\eta}$, i.e. NIWs have no linear potential vorticity. The fields describing the jet only depend on y. They are written down below:

$$u(y) = u_0 \mathrm{e}^{-y^2/\sigma_y^2}, \tag{3.2}$$

$$v(y) = 0, \tag{3.3}$$

$$\eta(y) = -\frac{Hy}{f_0\sigma_y^2} u(y). \tag{3.4}$$

Reference simulation: no background flow

The first run is a reference simulation where NIWs evolve on their own, without any barotropic dipole. We use our two-layer shallow-water model. Figure 4a plots the time evolution of the wave velocity, $\boldsymbol{u}$, and of the interface height field, η. Figure 4b shows the energy time series for

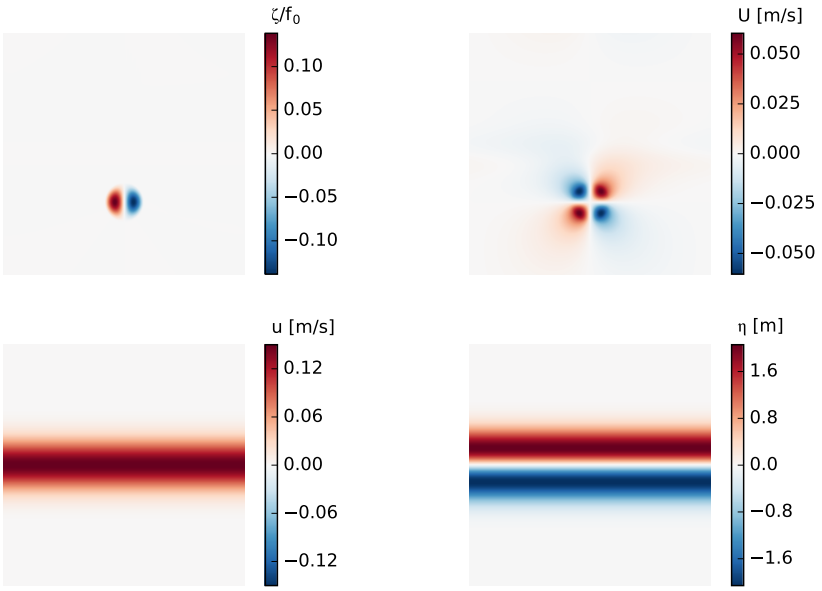

Figure 3: Initial fields of experiment D1. x- and y-axes correspond to the zonal and meridional directions, spanning 500 km × 500 km.

this reference simulation. E^W_{kin} has a large amplitude (nearly 100% of total energy), and so do E^W and E^{total} because they include E^W_{kin}. The three barotropic energy terms (E^ψ, E^ϕ and E^X), as well as E^G, are zero and stay zero. The right panel shows the same curves, but offset by their initial values, making small variations visible. The initial value considered is averaged over the first inertial period. High-frequency exchanges between kinetic and potential share a small part of the energy, about 0.8% of total energy. The wave typical wavenumber slightly increases with time, as shown in figure 4c. We used the baroclinic kinetic energy-weighted wavenumber, defined as

$$k_s = \frac{\int \kappa |\boldsymbol{u}(\kappa)|^2 \, \mathrm{d}\kappa}{\int |\boldsymbol{u}(\kappa)|^2 \, \mathrm{d}\kappa}. \tag{3.5}$$

A quick look back at the linearized one-layer shallow-water system (1.1-1.2) can enlighten us on the high-frequency exchanges between E^W_{pot} and E^W_{kin}. The kinetic energy evolution of the one-layer model goes like

$$\begin{aligned} KE_t &= \int \boldsymbol{u} \cdot \boldsymbol{u}_t \, \mathrm{d}s && (3.6)\\ &= \int \boldsymbol{u} \cdot (-f \hat{\boldsymbol{z}} \times \boldsymbol{u} - g \boldsymbol{\nabla} \eta) \, \mathrm{d}s && (3.7)\\ &= -g \int \boldsymbol{u} \cdot \boldsymbol{\nabla} \eta \, \mathrm{d}s && (3.8)\\ &= g \int \eta \, \boldsymbol{\nabla} \cdot \boldsymbol{u} \, \mathrm{d}s && (3.9) \end{aligned}$$

where, on the last line, an integration by parts was performed. Because total energy is conserved, this variation in the kinetic energy is balanced by the potential energy. We will now

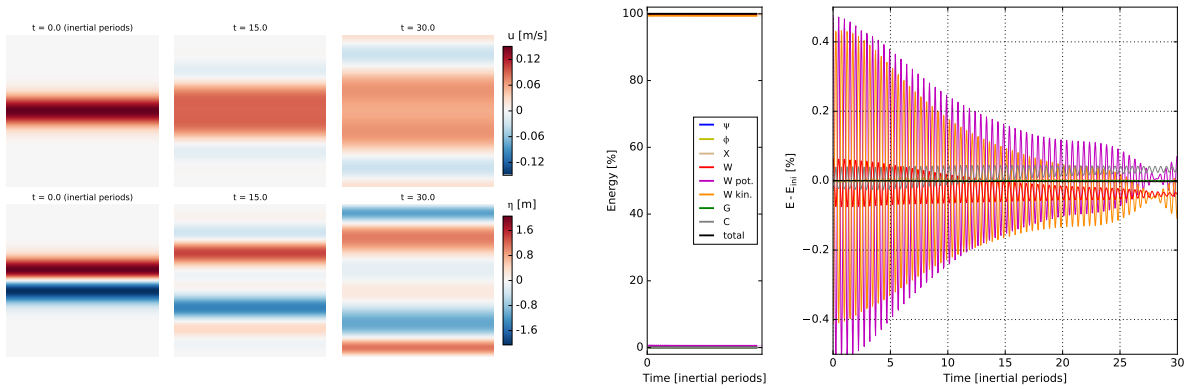

(a) Time evolution of u and η.

(b) Energy time series.

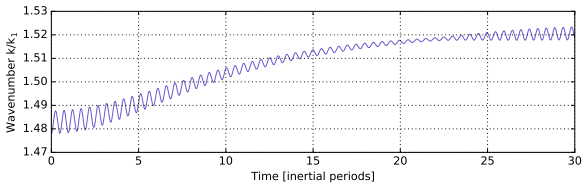

(c) Energy-weighted wavenumber.

Figure 4: Reference experiment with NIWs only. $L_d = 5$ km and $u_0 = 0.15$ m/s. In (a), x- and y-axes correspond to the zonal and meridional directions, spanning 500 km × 500 km.

make use of (1.7) and (1.8) in order to get rid of η and $\boldsymbol{\nabla} \cdot \boldsymbol{u}$ in our last expression. We then get

$$KE_t = g \int \left(\frac{H}{f}\zeta\right)\left(-\frac{1}{f}\zeta_t\right) \mathrm{d}s \tag{3.10}$$

$$= -\frac{gH}{f^2} \int \zeta\zeta_t \, \mathrm{d}s \tag{3.11}$$

$$= -L_d^2 \int \zeta\zeta_t \, \mathrm{d}s \tag{3.12}$$

If we assume that ζ oscillates at a frequency f, we find that KE_t is

$$KE_t = -L_d^2 \int \zeta_0^2(\boldsymbol{x}) \sin(ft)\cos(ft) \, \mathrm{d}s \tag{3.13}$$

$$= -\frac{L_d^2}{2} \int \zeta_0^2(\boldsymbol{x}) \sin(2ft) \, \mathrm{d}s \tag{3.14}$$

Considering a ballpark estimate for KE to be $L_W^2 \int \zeta_0^2(\boldsymbol{x}) \, \mathrm{d}s$, we find that

$$\frac{KE_t}{KE} \sim \frac{L_d^2}{L_W^2} \sin(2ft) \sim 0.003 \sin(2ft) \tag{3.15}$$

where we have taken the wave scale L_W to be 100 km. Therefore, our quick estimate produces an energy exchange between E^W_{pot} and E^W_{kin} very similar in frequency and in amplitude to figure 4.

Table 1: Parameters for the dipole experiments. L_0 is defined as $1/k_s$, where k_s is the barotropic kinetic energy weighted wavenumber. For all experiments, $f_0 = 10^{-4}$ s^{-1}.

Experiment:	**D1**	**D2**	**D3**	
$n_x \times n_y$	256^2	256^2	512^2	grid size
$L_x \times L_y$	$(500\text{ km})^2$	$(500\text{ km})^2$	$(1500\text{ km})^2$	domain size
H_t	160 m	160 m	1000 m	domain thickness
ν (10^{-6})	1.5 m^4/s	1.5 m^4/s	7.5 m^4/s	biharmonic viscosity
L_d	5 km	5 km	30 km	deformation radius
U_0	0.05 m/s	0.1 m/s	1 m/s	dipole velocity
r_{dip}	40 km	40 km	120 km	dipole radius
y_{dip}	-0.2 L_y	-0.2 L_y	-0.2 L_y	dipole position
u_0	0.15 m/s	0.15 m/s	0.25 m/s	NIWs velocity
σ_y	50 km	50 km	250 km	NIWs width
Ro_{max}	0.14	0.28	0.92	Rossby number
L_0	15 km	15 km	45 km	typical length scale

First dipole experiment (D1): XV-like

For the first run (D1), we picked the exact same parameters used by XV. This corresponds to a weak dipole, weak stratification, and strong waves. All parameters are specified in table 1. Results for this set-up are shown in figure 5, using both our two-layer shallow water model and XV generalized-Lagrangian-mean model (glm). Recall that governing equations for the glm model are (1.11) and (1.18).

During the simulation, the dipole crosses the domain once (figure 5a). It almost goes along an straight line, slightly turning west along its way. The dipole streamfunction stays stable and does not break apart. The baroclinic velocity $\boldsymbol{u}$ is basically just the wave velocity – baroclinic geostrophic currents are negligible. The wave field is strongly perturbed by the dipole, although its final characteristic length scale is comparable to its initial value (figure 5c, bottom panels). The energy redistributes itself in Fourier space, but does not move much to higher wavenumbers. Rather, the energy wave vector orientation is changed and the spatial distribution of NIWs becomes isotropic.

The velocities resulting from our two-layer model are virtually identical to those produced by the glm model, both with our implementation (figure 5c) of their equations or with figure 4 of XV. But even if the eye could not distinguish any difference in the velocity fields, the energy time series are still very different.

Figures 5b shows the energy time series for the two-layer model. Notice that any change to an energy term is small, under 0.5% of total energy. At first, the potential energy goes down as the waves disperse, just like in the reference run. Afterwards, when the dipole hits the waves, the potential energy goes up, mainly at the expense of the wave kinetic energy. One can also notice a small dip in E^C around $t = 15$ inertial periods, a feature that will be also present in the latter experiments D2 and D3. A little later in time, when the wave scale reaches a maximum

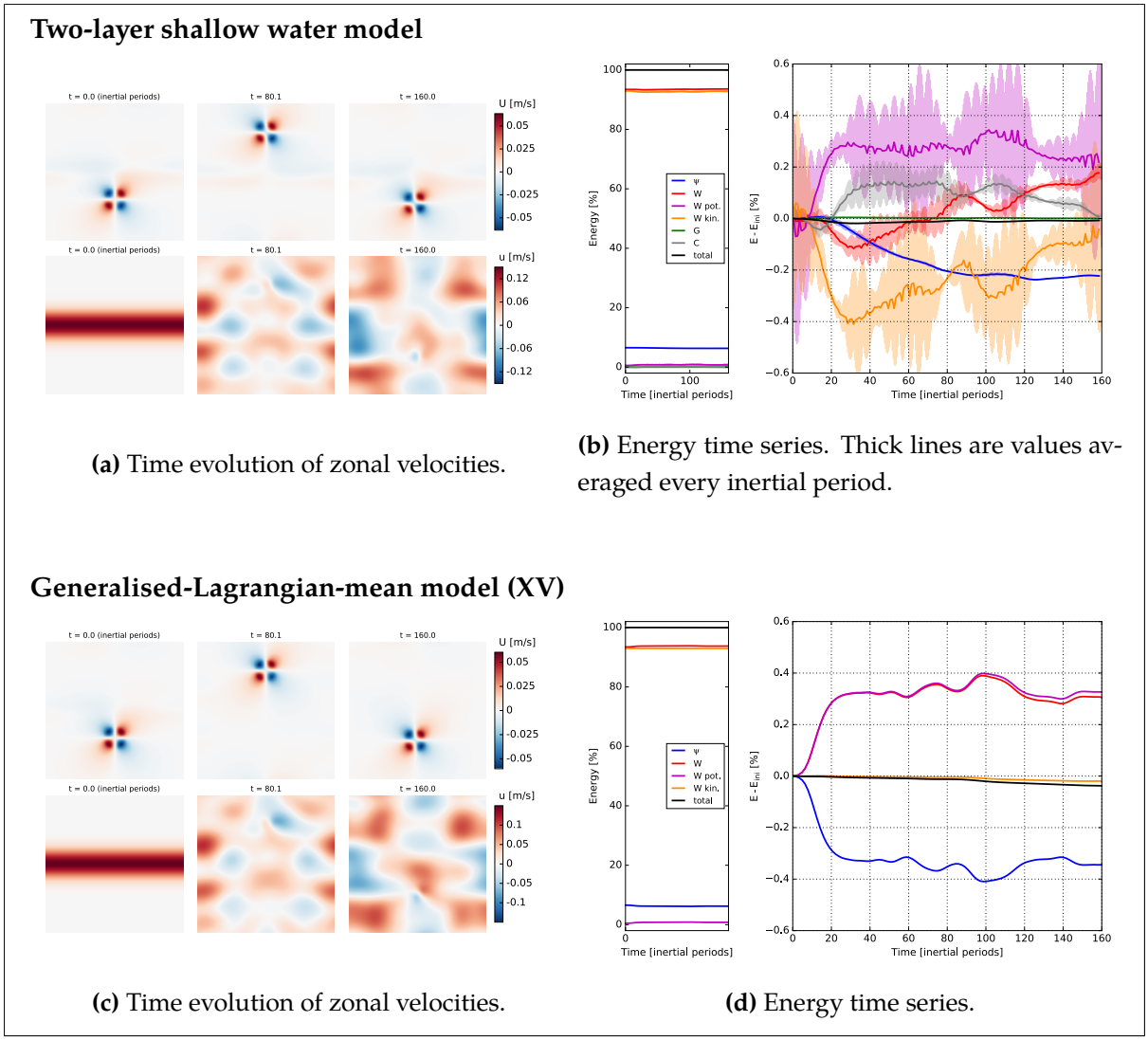

(a) Time evolution of zonal velocities.

(b) Energy time series. Thick lines are values averaged every inertial period.

(c) Time evolution of zonal velocities.

(d) Energy time series.

Figure 5: Experiment D1. $L_d = 5$ km, $U_0 = 0.05$ m/s and $u_0 = 0.15$ m/s. In (a) and (c), x- and y-axes correspond to the zonal and meridional directions, spanning 500 km × 500 km.

(c.f. figure 6) and the wave potential energy stops growing, the "cubic" energy term increases, and the wave kinetic energy goes down a little. Also, E^{ψ} begins to decrease at that time, a reduction that will continue to get larger until 100 inertial periods into the simulation. Notice that the wave action, proportional to E^{W}_{kin}, is not conserved in the two-layer model. E^{ϕ} and E^{X} are extremely small, and were not plotted. In fact, those two components of the energy budget will be very small for every experiment conducted in this thesis, so we will not show their time series from now on.

The glm model gives a very different portrait (figure 5d). The balanced energy goes down very cleanly, at the expense of the wave potential energy. Most of the transfer takes place between $t = 5$ and 25 inertial periods. The wave kinetic energy is conserved, as is the total energy. The transfer amplitudes are of the same order in both models. Figure 5d is a perfect copy of the results reported in XV, giving us confidence in our implementation of their equations.

This first look at these results leads us to observe that: i) both models produce virtually

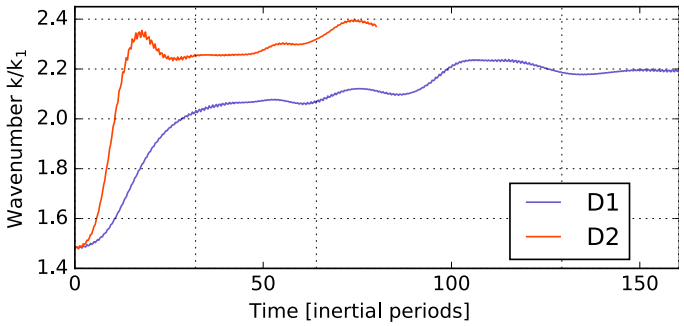

Figure 6: Comparison of the baroclinic kinetic energy-weighted wavenumbers for experiments D1 (U_0=0.05 m/s) and D2 (U_0=0.1 m/s).

the same flow, ii) both models show E^ψ going down, iii) both models show E^W_{pot} going up, and iv) the two-layer model sees the wave action conservation broken. We also take notice that the NIW length scale does not reduce much during the integration. Recall that a reduction in scale of the NIWs and a concomitant increase in the wave potential energy is at the core of the "stimulated generation" mechanism described by XV.

Second dipole experiment (D2): stronger dipole

We doubled the dipole velocity, up to $U_0 = 0.1$ m/s. According to theory, the NIW scale should decrease more, as waves are distorted by a stronger background flow. The NIW scale is indeed reduced to a smaller value, confirmed *a posteriori* by figure 6. Also, a factor-2 change in a parameter does not put us off the parameter space where XV's model is valid. Figure 7 shows the results for experiment D2. The simulation duration is 80 inertial periods, enough time for the dipole to cross the domain once.

Figures 7a and 7c are broadly similar to figures 5a and 5c. A noteworthy difference is that the NIW length scale now goes to higher wavenumbers, and it reaches small scales quicker (also c.f. figure 6). The smaller features are in the vicinity of the dipole.

The big difference with D1 lies in the energy times series. At about 10 inertial periods into the simulations, the dipole hits the NIW jet. In the two-layer model, E^W_{pot} quickly undergoes a threefold increase, at the expense of E^C. Meanwhile, E^W_{kin} is approximately conserved. Once the NIW scale has reached its maximum value, E^W_{pot} stabilizes and even goes down a little, as does the NIW scale (see figure 6). Also, during the same time period (between t = 15 and 30 inertial periods), E^C goes back up to reach its initial value and E^ψ decreases. In the second half of the integration, it becomes clear that the net transfer of energy has been from E^ψ to E^W_{pot}.

The glm model exhibits very similar energy time series compared to the previous weak-dipole experiment D1. The exchange amplitude is now a bit bigger, up to a maximal value of 0.6%. But now, most importantly, both models show energy time series (figures 7b and 7d) with striking resemblances. The two-layer model time series for E^C and E^ψ (blue and gray curves on figure 7) add up to an amount very similar to the glm model time series for E^ψ. Recall that in the two-layer framework, E^C is the kinetic energy associated with the interface deformation.

Two-layer shallow water model

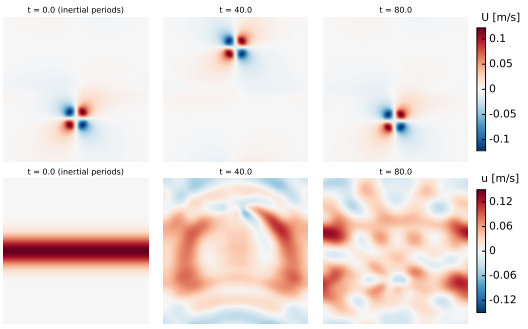

(a) Time evolution of zonal velocities.

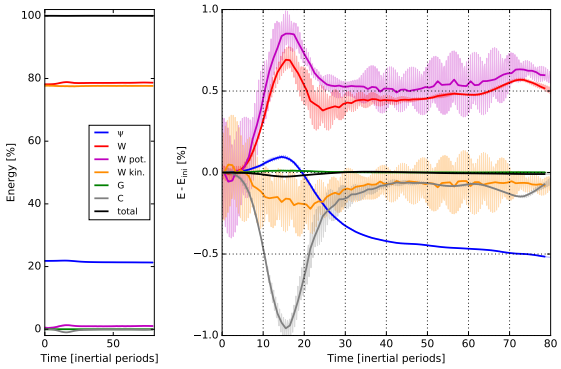

(b) Energy time series. Thick lines are values averaged every inertial period.

Generalised-Lagrangian-mean model (XV)

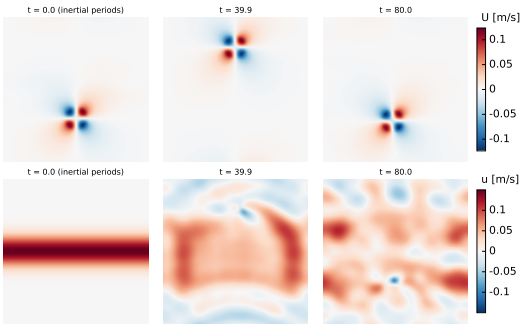

(c) Time evolution of zonal velocities.

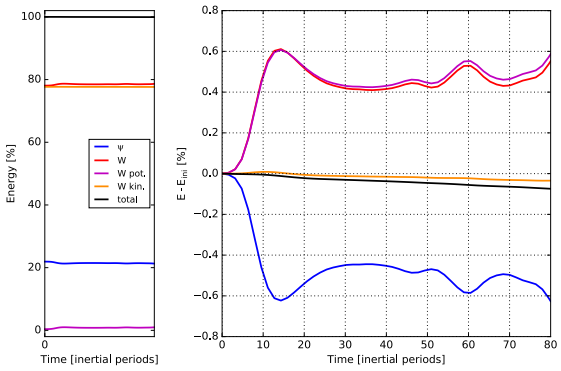

(d) Energy time series.

Figure 7: Experiment D2. L_d = 5 km, U_0 = 0.1 m/s and u_0 = 0.15 m/s. In (a) and (c), x- and y-axes correspond to the zonal and meridional directions, spanning 500 km × 500 km.

E^C should not be associated with baroclinic or barotropic energy – it is more like the correction between these two modes. In experiment D2, energy would go from E^C to E^W_{kin} at first, before moving from E^ψ to E^C later. Notice that E^C has no equivalent in the glm model. Therefore, even if the final energy transfer is similar with both models, it seems like the mechanism is not the same. We nonetheless acknowledge that our model reproduces the results from the glm model, aside from the difference in E^C. A more detailed comparison, and ideas to explain why the concordance between models is not as good in D1, is offered in the discussion section.

Third dipole experiment (D3): "realistic" parameters

The parameters chosen by XV had to correspond to small Ro and Bu numbers in order to satisfy to the approximations behind the glm model. Since our two-layer model does not have these limitations, we can study the transfers between NIWs and the balanced flow with

a stronger flow and stronger stratification. We selected the new parameters with the intention of representing reality more accurately. We used synoptic-scale NIWs with a size of many hundreds of kilometers. Initial conditions for waves are still in the shape of a jet. They instantaneously appear at time $t = 0$, as before. This choice is not so unrealistic: when storms blow wind and put the upper layer of the ocean in movement, it acts on a very short time scale, i.e. a few hours (Alford et al., 2016). Although working on a now bigger domain (1500 km $\times$ 1500 km), we remain on a f-plane. Thinking of the Gulf Stream as of our reference background flow, we choose a maximal velocity of $O(1\text{ m/s})$ and a maximal vorticity of about $O(f_0)$. Stratification is more representative of the reality when $L_d = 30$ km is used. Detailed parameters for experiment D3 are in table 1.

This experiment is outside of the parameter space formally assumed for the glm model. We nonetheless tried to run a simulation of experiment D3 with XV's model, expecting that the results would not be reliable.

As with experiments D1 and D2, the dipole again goes north, here with a negligible deflection caused by waves (figure 8a). Some baroclinic geostrophic currents are also excited, especially at about 5 inertial periods into the simulation (middle panels of 8). These baroclinic geostrophic currents follow the dipole as it moves. Their length scale is very small. Like in the previous experiments D1 and D2, the NIWs jet is broken and waves cover all the domain isotropically. NIWs see a reduction in their length scale, down to some very small features in the vicinity of the dipole. Take note that the scale to which NIWs go down is limited by the deformation radius. Waves retain their near-inertial character, and therefore their scale is obeying to the dispersion relation (1.10).

The wave velocity field obtained with the glm model (8c) is qualitatively similar to the field produced by the two-layer model, but differences are now obvious. Differences are especially important in the vicinity of the dipole, as the glm model does not enables baroclinic geostrophic currents.

The energy time series (figure 8b) shows a significant increase in the wave potential energy as the dipole impinges on the waves. This increase goes along with a decrease in E^C, E^W_{kin} and E^ψ during the first ten inertial periods. Later on, E^C and E^W_{kin} go back up, but E^ψ remains below its initial value. As before, we see a net transfer from $E^\psi \rightarrow E^W_{\text{pot}}$, with E^C serving as an intermediate reservoir. However, in D3, this mechanism is not working alone. Indeed, the final value of E^ψ is well under the lowest energy level reached by E^C. There thus must be a mechanism that transfers energy directly from E^ψ to E^W_{pot}.

The energy time series for the glm model (figure 8d) are reminiscent of previous experiments D1 and D2. They differ from the results of the two-layer model by their absence of baroclinic geostrophic energy and their conservation of the wave action.

This last experiment most importantly teaches us that the energy transfer from the balanced flow to the waves takes place even with more realistic parameters, i.e. at higher Ro and with stronger stratification. It is very interesting that the energy transfer is robust to a variety of parameters, with the only condition of a decrease in the NIW length scale.

Two-layer shallow water model

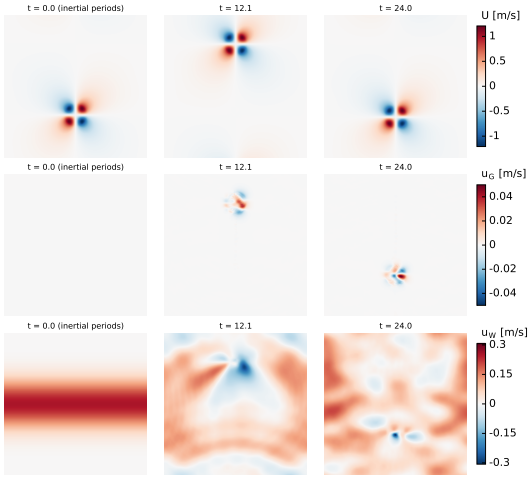

(a) Time evolution of zonal velocities.

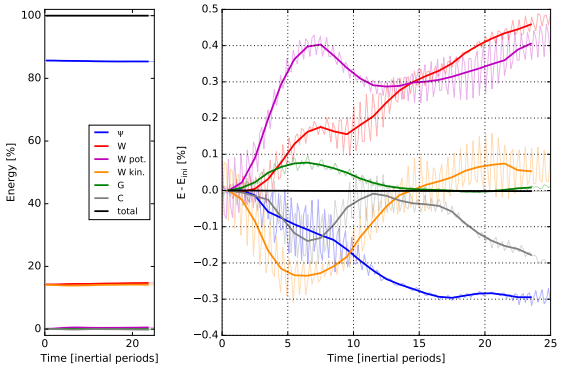

(b) Energy time series. Thick lines are values averaged every inertial period.

Generalised-Lagrangian-mean model (XV)

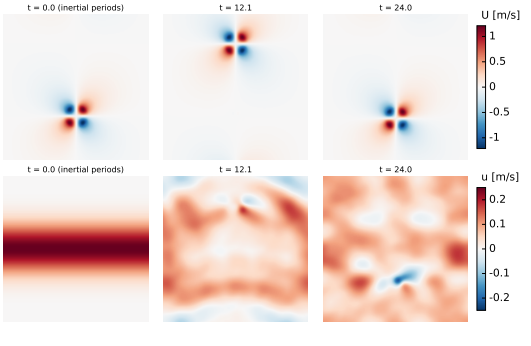

(c) Time evolution of zonal velocities.

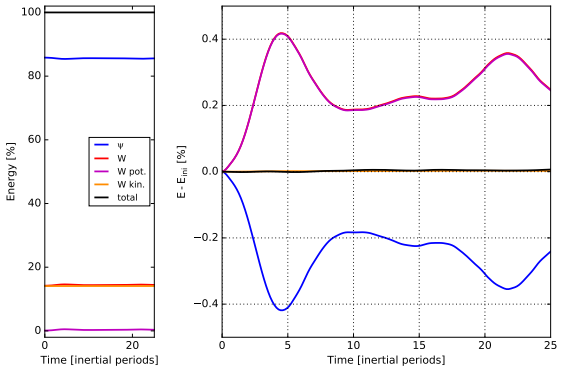

(d) Energy time series.

Figure 8: Experiment D3. L_d = 30 km, U_0 = 1 m/s and u_0 = 0.25 m/s. In (a) and (c), x- and y-axes correspond to the zonal and meridional directions, spanning 1500 km × 1500 km.

Time evolution of the balanced flow

Previous sections exposed the energy time series for experiments D1, D2 and D3. Although this gave us an intuition on how the energy changes reservoir, it did not tell us with certainty how the energy transfers work. With the use of the energy evolution equation, we can pin down the origin of energy transfers. That is what we will do in this section.

Figure 9 shows how the different forcing terms impact the energy equations of the balanced flow. In the dipole experiments, E^G is very small and will not be considered. E^ψ is influenced by W, G, ϕ and ψ according to equations (2.58) through (2.62). The forcing terms are integrated in time and shown as energy time series. Each integrated forcing term corresponds to the change in E^ψ if no other forcing were considered. The sum of all non-zero contributions to a balanced mode make up the energy time series as calculated with the energy budget equation.

In experiment D1, the evolution of E^ψ is subject to the strong forcing of ${}^{\phi}E^{\psi}$ and ${}^{WW}E^{\psi}$ (figure 9a). These two terms are broadly of equal amplitude and of opposite sign, therefore approximately canceling. The bottom panel of figure 9a shows the sum ${}^{\phi}E^{\psi} + {}^{WW}E^{\psi}$ (light blue curve). ${}^{\phi\psi}E^{\psi}$ (pink) is the most significant contribution to the change in E^ψ. We will later argue that ${}^{\phi\psi}E^{\psi}$ is a transfer term that carries energy between E^ψ and E^C. We finally take notice that the sum of the five contributions to E^ψ does not match perfectly with the time series for E^ψ. This discrepancy might be caused by the time stepping scheme which is not the same for the model and for computing the energy evolution contribution. For the model, we use a "leap-frog" time stepping scheme, which is more accurate, while E^ψ_t is computed with a simple Euler scheme.

In experiment D2 (figure 9b), there is once again a clear forcing competition between ${}^{\phi}E^{\psi}$ and ${}^{WW}E^{\psi}$, each one pushing with a strength that would change the energy by an amount of 10% if it were not balanced. On the bottom panel, one sees that, as before, ${}^{\phi\psi}E^{\psi}$ is very important to explain the decrease in E^ψ. ${}^{\phi\psi}E^{\psi}$ first increases while the dipole enters in contact with the NIWs. It afterwards goes down, when the dipole moves away.

Figure 9c is the reconstructed energy time series for experiment D3, the run with "realistic" settings. We see the same kind of pattern, in which ${}^{\phi}E^{\psi}$ and ${}^{WW}E^{\psi}$ are similar in amplitude and opposite in sign. However, it is now the sum of ${}^{\phi}E^{\psi}$ and ${}^{WW}E^{\psi}$ that fits with good agreement to the decrease in E^ψ. The experiment D3 also features a change in the other balanced energy term, E^G. It is mostly ${}^{\psi W}E^{G}$ that produces the transfer from E^ψ to E^G (not shown).

In the discussion section, we will try to shed light on the issues raised by the inspection of the balanced flow time evolution. We will see that ${}^{\phi\psi}E^{\psi}$ has a complement (labeled ${}^{(\phi\psi\psi)}E^{C}$) such that

$$ {}^{\phi\psi}E^{\psi}_t + {}^{(\phi\psi\psi)}E^{C}_t \simeq 0. \tag{3.16} $$

We will see that this complement is indeed transferring energy between E^ψ and E^C. The energy transfer between the NIWs and the balanced flow is therefore indirect and goes through E^C. Very interestingly, we will see in the next section that E^C is not as important when the background flow is turbulent.

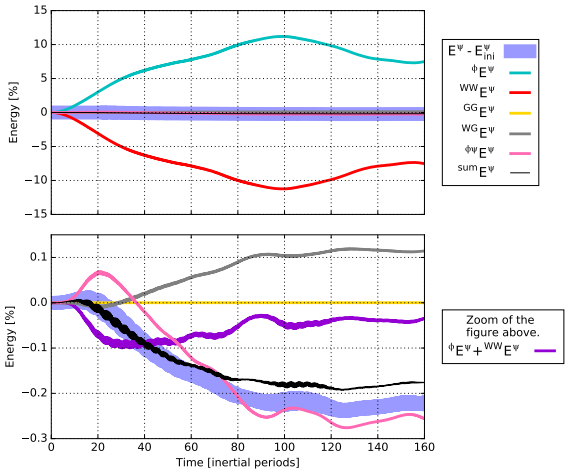

(a) Experiment D1.

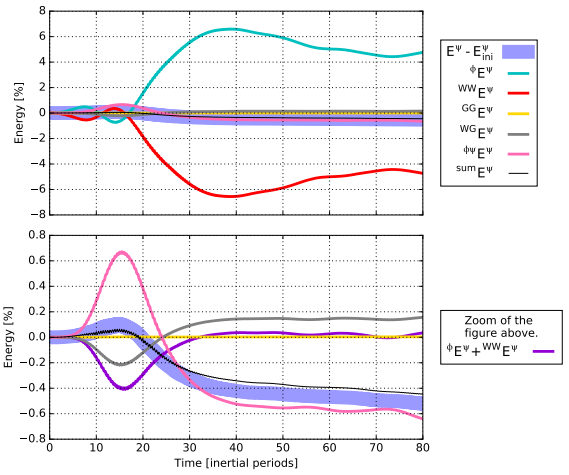

(b) Experiment D2.

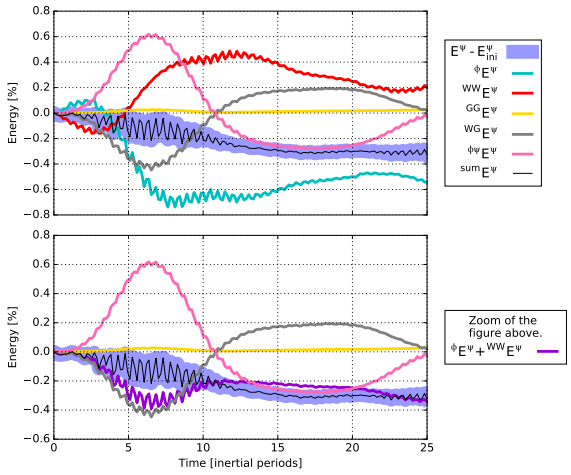

(c) Experiment D3.

Figure 9: Balanced energy time series, reconstructed with the energy-evolution equations for each mode.

3.2 Turbulent flows

We will next use turbulence instead of a dipole as initial conditions for the barotropic flow. This background flow choice is closer to reality. Also, no specific "event", like the encounter between the dipole and waves, will happen with an isotropic and uniform turbulent field. This will help us draw conclusions not specific to a particular geometrical set-up. The mature turbulent flow is obtained after the spin-up of a two-dimensional flow with random initial phases and small wavelengths. The mature flow exhibits turbulent features with a scale of 41 km. The domain has a size of 1500 km × 1500 km, and is still doubly periodic. Over the background flow, we initially superimpose NIWs with a Gaussian profile along the meridional direction. All parameters for T1, and for the other turbulent experiments, are detailed in table 2.

Table 2: Parameters for the turbulent experiments. L_0 is defined as $1/k_s$, where k_s is the barotropic kinetic energy weighted wavenumber. For all experiments, $f_0 = 10^{-4}$ s^{-1}.

Experiment:	**T1**	**T2**	**T3**	
$n_x \times n_y$	512^2	512^2	512^2	grid size
$L_x \times L_y$	$(1500\text{ km})^2$	$(1500\text{ km})^2$	$(1500\text{ km})^2$	domain size
H_t	1000 m	1000 m	1000 m	domain thickness
ν (10^{-6})	7.5 m^4/s	7.5 m^4/s	7.5 m^4/s	biharmonic viscosity
L_d	15 km	30 km	50 km	deformation radius
U_0	1 m/s	1 m/s	1 m/s	turbulence velocity
u_0	0.25 m/s	0.25 m/s	0.25 m/s	NIWs velocity
σ_y	250 km	250 km	250 km	NIWs width
$\mathrm{Ro}_{\max}$	0.52	0.52	0.52	Rossby number
L_0	41 km	41 km	41 km	typical length scale

First turbulent experiment (T1): weak stratification

Experiment T1 aims to highlight the energy transfer caused by a scale reduction in NIWs, a phenomenon that was first pointed out by XV and that we reproduced in the previous results. To do so, we chose a small deformation radius (15 km) compared with the typical scale of the barotropic flow (41 km). Figure 10a shows zonal velocity fields. U evolves like a normal 2d turbulent flow and its typical length scale enlarges with time. u_G is excited at very small scales and with negligible amplitude (not shown). Waves, initially in a Gaussian shape, quickly become isotropic and reach very small scales. This very significant scale reduction is the reason for an increase in E^W_{pot} larger than what we saw in experiments D1, D2 and D3.

In figure 10b, energy time series are plotted. The wave potential energy increases with time to reach more than 2% of total energy after 100 inertial periods. Keeping in mind that the wave kinetic energy constitutes just 8% of total energy, this represents a 25% increase in the wave energy. The wave kinetic energy remains approximatively constant. The barotropic divergenceless energy decreases, as does E^C. Both time series decrease monotonically and with a broadly constant slope.

It is now very clear that energy coming from the balanced flow increases the wave potential energy, although it is unclear whether E^C plays an intermediary role in the transfer. The conservation of wave action in Experiment T1 is remarkable. After a small dip in the first 10 inertial periods, E^W_{kin} (proportional to the wave action) is increasing with a very gentle slope. Variations in E^W_{kin} are much smaller than those in E^W_{pot} or E^ψ.

Second turbulent experiment (T2): medium stratification

In this next experiment, stratification is increased to a value characteristic of the mid-latitude ocean jets (L_d = 30 km). This is still smaller than the typical background flow scale (41 km). A stronger stratification should stop the NIW cascade before it reaches scales as small as in T1, as indicated by dispersion relation (2.6). We expect this would reduce the energy transfer

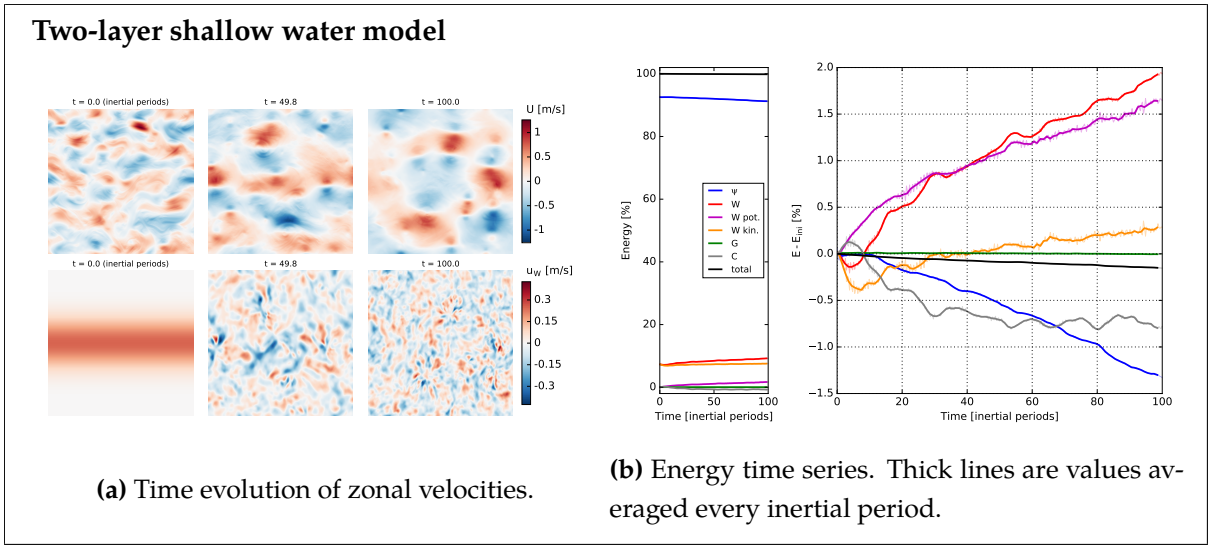

(a) Time evolution of zonal velocities.

(b) Energy time series. Thick lines are values averaged every inertial period.

Figure 10: Experiment T1. $L_d = 15$ km, $U_0 = 1$ m/s and $u_0 = 0.25$ m/s. In (a), x- and y-axes correspond to the zonal and meridional directions, spanning 1500 km $\times$ 1500 km.

from the balanced flow to NIWs. We will also find that a new energy transfer happens in this simulation.

Figure 11a shows that U is behaving like before, and its length scale grows with time. But here, baroclinic geostrophic currents are not negligible any more (middle panel of 11a). They develop at small length scales. On the other hand, waves exist predominantly at large scale. The length scale cascade stopped early, as anticipated.

Figure 11b shows energy time series for experiment T2. There is still a small increase in the wave energy, carried by the potential energy. The baroclinic geostrophic energy is also building up, a feature that we did not observe before. E^ψ is going down, feeding both baroclinic geostrophic currents and waves. The wave action, equal to E^W_{kin}/f_0, oscillates in time with a small amplitude. As stratification is increased, it more strongly perturbs the NIW phase and breaks the conditions for the conservation of wave action.

Third turbulent experiment (T3): strong stratification

We will now use a stronger stratification, that is a larger deformation radius. $L_d = 50$ km is now larger than the scale of the barotropic flow $L_0 = 41$ km. This will highlight the transfer mechanism taking energy from the barotropic mode to feed E^G.

Figure 12a shows the different velocity fields of the experiment. In the top panel, U undergoes the usual inverse-cascade, without visible perturbation by the wave field. The middle panel is the baroclinic geostrophic velocity, which is of significant amplitude. It grows from zero, and acquires a turbulent shape, with a small length scale. Finally, the bottom panel is the wave velocity. It keeps a large characteristic length scale (compare with 7a).

Figure 12b presents the energy time series of experiment T3. While variations in the wave potential and kinetic energies are just like in experiment T2, E^G increases. Both the potential

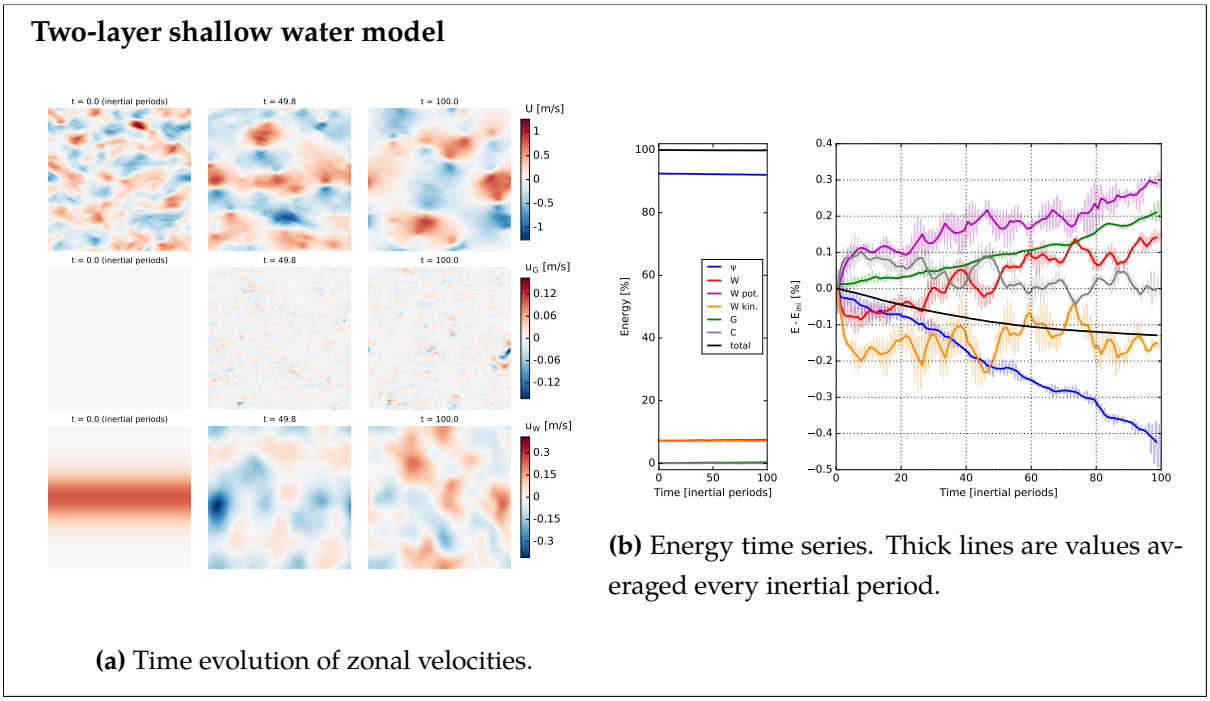

(a) Time evolution of zonal velocities.

(b) Energy time series. Thick lines are values averaged every inertial period.

Figure 11: Experiment T2. L_d = 30 km, U_0 = 1 m/s and u_0 = 0.25 m/s. In (a), x- and y-axes correspond to the zonal and meridional directions, spanning 1500 km × 1500 km.

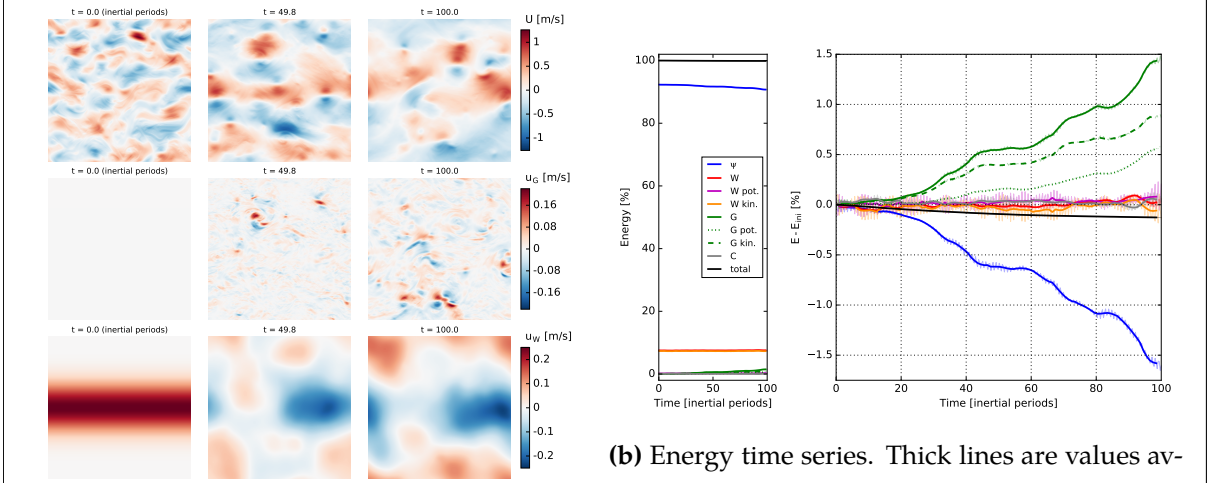

(a) Time evolution of zonal velocities.

(b) Energy time series. Thick lines are values averaged every inertial period.

Figure 12: Experiment T3. L_d = 50 km, U_0 = 1 m/s and u_0 = 0.25 m/s. In (a), x- and y-axes correspond to the zonal and meridional directions, spanning 1500 km × 1500 km.

and kinetic parts of E^G are becoming more significant, at the expense of E^ψ.

Recall that the turbulent cascade is also at play in the vertical direction and not only in the horizontal plane. There is normally a "barotropisation" of the flow where the baroclinic modes give up energy to the barotropic flow (see the Kolmogorov theory in Vallis (2006)).

One could think the increase in E^G is remarkable because it opposes to the expected inverse-cascade towards larger vertical wavenumbers. However, a simple argument can explain the "baroclinisation" of the flow: because the baroclinic geostrophic mode is initially zero, it has no choice but to grow. As long as there is some energy transfer terms mixing the baroclinic geostrophic currents and ψ, namely ${}^{GG}E^\psi$, the baroclinic geostrophic energy will not stay zero. Small amplitude energy exchanges between waves and baroclinic geostrophic currents are able to trigger an amplification of the baroclinic geostrophic currents supplied in energy by E^ψ. Although this phenomenon is interesting, it is not directly relevant to our study of transfers from the balanced flow to NIWs, and will not be considered further.

Time evolution of the balanced flow

We now turn our attention to the time evolution of the balanced modes ψ and G. Figure 13 breaks down the energy evolution equation for the balanced modes in experiments T1, T2 and T3. This should help us to better understand energy transfers between the fast modes and the balanced modes.

Experiment T1 exhibits a strong forcing competition between ${}^{\phi}E^\psi$ and ${}^{WW}E^\psi$ (figure 13a). We saw the same thing for the other dipole experiments. When ${}^{\phi}E^\psi$ and ${}^{WW}E^\psi$ are added up (bottom panel) they are the main contribution to the decrease of the barotropic energy. See the discussion section for a more complete analysis of the energy transfers of experiment T1. Also notice that ${}^{\phi\psi}E^\psi$ (pink curve) is not transferring energy to E^ψ, but instead taking energy from it.

Figure 13b presents experiment T2, where the decrease in E^ψ contributes both to the baroclinic geostrophic and wave modes. The sum of ${}^{\phi}E^\psi$ and ${}^{WW}E^\psi$ still does most of the energy transfer to the waves. It is the forcing term ${}^{GG}E^\psi$ that causes the transfer from E^ψ to E^G. The mixed action of two mechanisms ($E^\psi \rightarrow E^W$ and $E^\psi \rightarrow E^G$) that we see in the energy time series (figure 11b) is easily identified here. On the bottom panel of figure 13b, the time evolution of E^G is plotted. ${}^{\psi W}E^G$ is doing some small-amplitude and low-frequency transfers between waves and baroclinic geostrophic currents. During the first 20 inertial periods, it is ${}^{\psi W}E^G$ that makes up the increase to E^G. Afterwards, ${}^{\psi G}E^G$ kicks in and increases more significantly E^G. This term is complementary to ${}^{GG}E^\psi$ in the energy evolution equation of E^ψ.

For experiment T3, figure 13c shows very clearly that when the typical scale of the background flow is smaller than the deformation radius, the baroclinic geostrophic energy increases via ${}^{\psi G}E^G$ and the barotropic energy decreases via ${}^{GG}E^\psi$. No energy is transfered to NIWs from E^G. We expect that if the simulation lasted long enough, E^G would reach a plateau before going back down, according to the process of barotropisation.

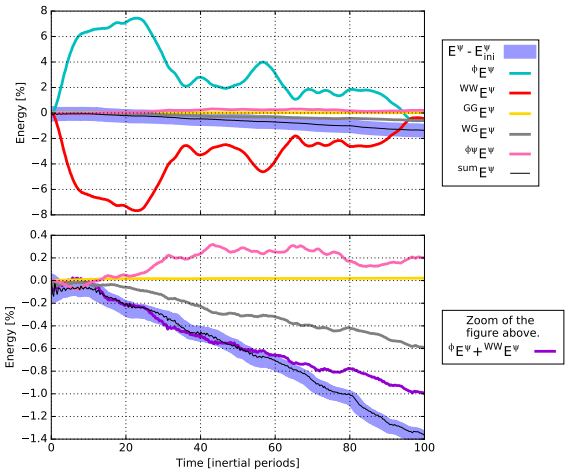

(a) Experiment T1.

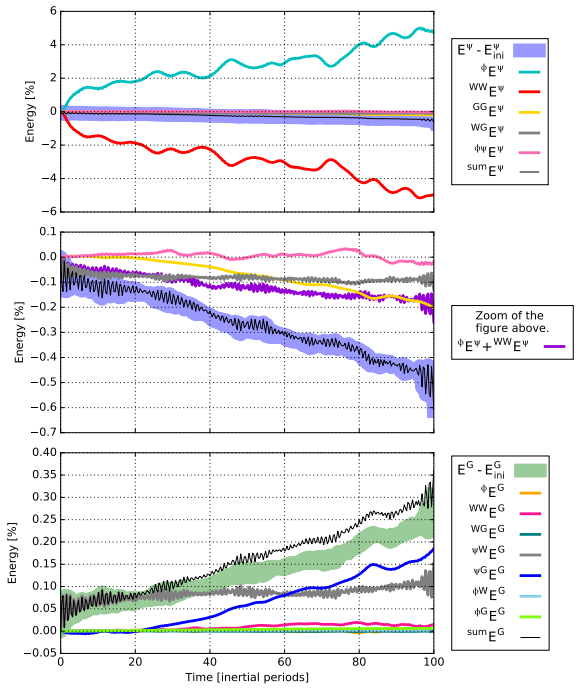

(b) Experiment T2.

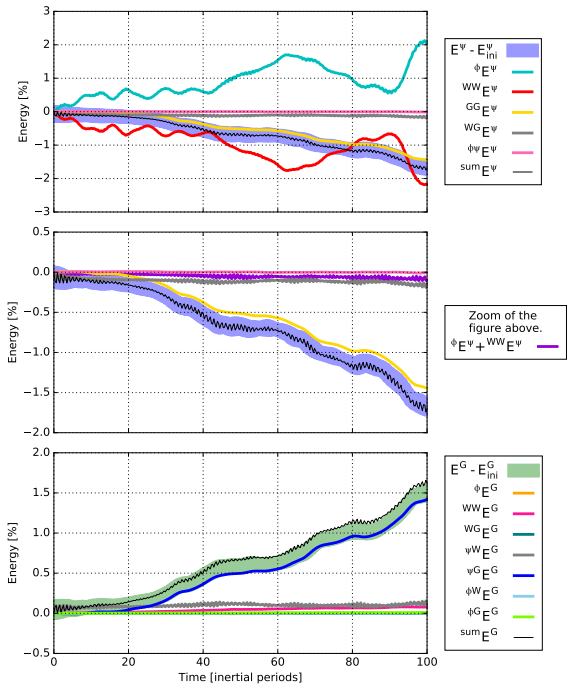

(c) Experiment T3.

Figure 13: Balanced energy time series, reconstructed with the energy-evolution equations for each mode.

Chapter 4

Discussion and Conclusion

4.1 Dipole experiments: comparison between models

We now will try to understand the similarities and differences between the two-layer shallow-water model and the generalised-Lagrangian-mean model (glm) using experiments D1 and D2. Experiment D1 is the original numerical experiment performed in XV. Although the velocity fields produced by both models are virtually the same, the energy time series look very different. In experiment D2, where the background flow is twice as strong, the two-layer model gives results closer to those produced by the glm model. We will try to understand why.

Generalised-Lagrangian-mean model

In both D1 and D2, the glm model exhibits the "stimulated wave generation" identified by XV, where the wave potential energy increases at the expense of the barotropic energy:

$$E^{\psi} \rightarrow E^{W}_{\text{pot}}. \tag{4.1}$$

Two-layer shallow-water model

Our two-layer model also is characterized by an increase of E^{W}_{pot}, but energy is not coming only and directly from E^{ψ}. The two-layer framework allows the kinetic energy to change depending on the interface deformation through the term E^{C}. Our results with the two-layer model (figures 5b, 7b) suggest that changes in E^{C} are not negligible and have an appreciable impact on the global energy budget.

Experiment D1, conducted with the two-layer model, significantly differs from the same simulation made with the glm model (c.f. figure 5d). The two-layer model takes energy from the wave kinetic energy to increase E^{W}_{pot}. Transfers are such that

$$\text{early on } E^{W}_{\text{kin}} \rightarrow E^{W}_{\text{pot}}, \tag{4.2}$$

$$\text{and later } E^{W}_{\text{kin}} \leftarrow E^{\psi}. \tag{4.3}$$

E^{C} also varies in time, but with a lesser net impact on E^{ψ}.

Experiment D2 gives similar results with both models if we think of E^C as an intermediary between E^ψ and E^W_{pot}. Transfers are such that

$$\text{early on } \; E^C \rightarrow E^W_{\text{pot}}, \tag{4.4}$$

$$\text{and later } \; E^C \leftarrow E^\psi. \tag{4.5}$$

We are led to a simple observation, common to every experiment: when the wave scale shrinks, the wave potential energy has to go up. Where energy comes from seems to depend on the strength of the background flow. With weaker flows, energy comes from the wave kinetic energy, while with stronger flows, energy comes from the balanced flow after it was first supplied by E^C. We need to look more in details at E^C in the energy-evolution equations.

E^C as an intermediary

Figure 14 compares E^C (gray) with the reconstructed energy time series ${}^{\phi\psi}E^\psi$ (pink) for experiments D1 and D2. The two time series are broadly of opposite sign. It appears that ${}^{\phi\psi}E^\psi_t$ might represent a forcing that would take energy from E^C and would give it to E^ψ. We can even identify a term in the time-evolution equation for E^C that could be a complement of ${}^{\phi\psi}E^\psi_t$. We will use (2.47) for the evolution of $\boldsymbol{U}_t$ in Bernoulli-vorticity form. After integration by parts, we will make use of the definition of $\boldsymbol{U}_\phi$ to replace $\eta\boldsymbol{u}$ in our expression. The algebra is below:

$$E^C_t = +\frac{2}{H}\iint \boldsymbol{U}_t \cdot \eta\boldsymbol{u}\,\mathrm{d}\boldsymbol{x} + ... \tag{4.6}$$

$$= +\frac{2}{H}\iint \left(-\tfrac{1}{2}\boldsymbol{\nabla}|\boldsymbol{U}|^2\right) \cdot \eta\boldsymbol{u}\,\mathrm{d}\boldsymbol{x} + ... \qquad \text{using (2.47)} \tag{4.7}$$

$$= -\frac{1}{2}\iint |\boldsymbol{U}|^2\,\boldsymbol{\nabla}\cdot\left(-\tfrac{2}{H}\eta\boldsymbol{u}\right)\,\mathrm{d}\boldsymbol{x} + ... \qquad \text{integration by part} \tag{4.8}$$

$$= -\frac{1}{2}\iint |\boldsymbol{U}|^2\,\boldsymbol{\nabla}\cdot\boldsymbol{U}_\phi\,\mathrm{d}\boldsymbol{x} + ... \qquad \text{using (2.23)} \tag{4.9}$$

This part of E^C_t is cubic, where variables ϕ and ψ^2 make up the total product. Recall that $\boldsymbol{U}_\phi$ is very small, therefore $|\boldsymbol{U}|^2 \simeq |\boldsymbol{U}_\psi|^2$. Because E^C does not stem directly from an orthogonal variable – it is more like a cross-term – we cannot write its energy contributions like ${}^{\text{forcings}}E^C$. We will simply define the energy-transfer term

$${}^{(\phi\psi\psi)}E^C_t \equiv -\frac{1}{2}\iint |\boldsymbol{U}_\psi|^2\,\boldsymbol{\nabla}\cdot\boldsymbol{U}_\phi\,\mathrm{d}\boldsymbol{x}, \tag{4.10}$$

where the involved variables are between parenthesis as superscripts. ${}^{(\phi\psi\psi)}E^C_t$ is making up most of E^C in experiment D2 (red curve, figure 14b). From $t = 0$ to 15 inertial periods, ${}^{(\phi\psi\psi)}E^C_t$ is forcing an extraction of energy from E^C and giving it to E^ψ. However, this forcing has no net effect on E^ψ – energy is directly sent to E^W_{pot}. After $t = 15$ inertial periods, ${}^{(\phi\psi\psi)}E^C_t$ forces E^C back to its initial value, using the barotropic divergenceless energy, E^ψ. Energy is then effectively pumped from E^ψ. We will consider that experiment D2 exhibits XV's "stimulated wave generation", with the only difference being that energy has to go through E^C. We will now try to understand why experiment D1 is not behaving the same.

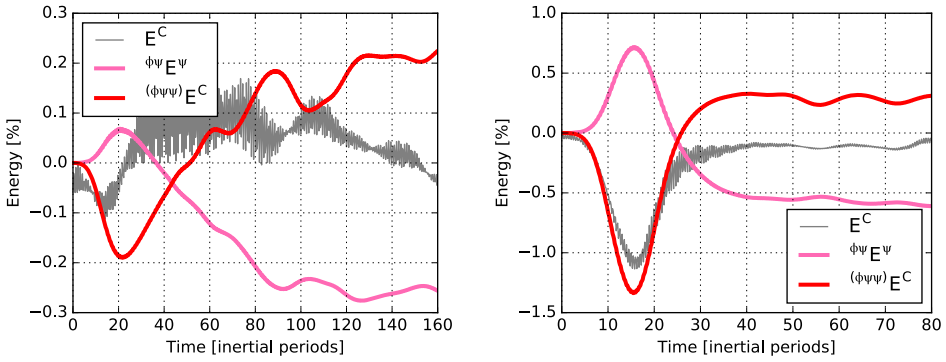

(a) Experiment D1. **(b)** Experiment D2.

Figure 14: Comparison between E^C, ${}^{\phi\psi}E^{\psi}$ and ${}^{(\phi\psi\psi)}E^C$.

In experiment D1 (figure 14a), E^C and ${}^{(\phi\psi\psi)}E^C$ do not fit together after $t = 5$ inertial periods. Notice that the E^C time series is very noisy – the amplitude of high-frequency oscillations is comparable to that of slow changes. It may be that the mechanism transferring energy from E^C to E^W_{pot} is not strong enough to overwhelm other fast-timescale fluctuations in E^C.

An hypothetical explanation for the difference between D1 and D2 would be that undulations in the interface height field, η, have to be large for E^C to change significantly. If so, E^C can give up some of its energy to increase the wave potential energy (D2, figure 7b). If not, because advection and refraction by the background flow are too weak, the energy that increases E^W_{pot} comes from E^W_{kin} instead of E^C (D1, figure 5b). Since E^W_{kin} varies, this breaks the wave action conservation.

Breaking of the wave action conservation

The wave action conservation of which XV make use might be not as robust as they suppose. One has to keep in mind that changes in wave action do not need to be large to balance the increase in E^W_{pot}. Wave action conservation requires the amplitude and phase of the wave to change slowly in time and space. According to linear theory, the difference between $u_\parallel$ and $u_\perp$, the amplitudes of NIWs along and across a background velocity gradient, should go like

$$\frac{u_\perp}{u_\parallel} = \sqrt{\frac{f_0}{f_0 + \zeta}}. \tag{4.11}$$

In experiment D1, ζ has a maximal amplitude of about $f_0/10$, yielding $u_\perp/u_\parallel \simeq 0.95$. This small asymmetry between $u_\perp$ and $u_\parallel$ changes the oscillation amplitude on a fast time scale. It weakly breaks the conditions for action conservation. It might be enough to cause a variation in the wave action of 0.4% (E^W_{kin} in figure 5). Even if this deviation from the conservation law might seem small, it has the same order of magnitude than other terms in the energy budget, and therefore is very significant. According to this argument, D2 would be even more susceptible to break the action conservation. Nonetheless, the transfer from the balanced flow takes over, in D2, and balances the increase in wave potential energy, maybe because of the stronger deformation in η.

4.2 Experiment T1: transfer from the background flow to the wave potential energy

In the previous section, we saw that energy could be transferred from the balanced flow to NIWs, with E^C as an intermediary step. However, we did not pay much attention to the mechanism extracting energy from NIWs. Experiment T1, in which energy goes from E^ψ to E^W_{pot}, without going through E^C, offers an insightful context to study this phenomenon.

In the following steps, we will need an expression for the baroclinic potential vorticity (PV). To obtain it, we will subtract the shallow-water PV of each layer, $q_{1,2} = (f \mp \zeta_2)(1/2 \mp \tilde{\eta})^{-1}$. We then find

$$q_2 - q_1 = \frac{\zeta_2 - 2f\tilde{\eta}}{1/4 - \tilde{\eta}^2}, \tag{4.12}$$

$$\simeq \zeta_2 - 2f\tilde{\eta}. \tag{4.13}$$

Such a linearisation of the baroclinic PV is a very good approximation of the complete baroclinic PV because the first order expansion of the denominator is zero. Recall from the derivation of the Poincaré wave dispersion relation that the linear PV of IGWs is zero, i.e., $\zeta_W = 2f\tilde{\eta}_W$. Therefore, all the baroclinic PV is contained in mode G. Thus, q_G corresponds to the baroclinic linear PV:

$$q^{\text{lin}}_{\text{bc}} = q_G \equiv \zeta_G - 2f\tilde{\eta}_G. \tag{4.14}$$

Recall that in all simulations (figures 9, 13), ${}^{\phi}E^{\psi}_t + {}^{WW}E^{\psi}_t \simeq 0$. We will now show why, using analytical methods. First, we will break down ${}^{\phi}E^{\psi}_t$, c.f. (2.61), into three parts:

$${}^{\phi_{\text{WW}}}E^{\psi}_t = f \iint \boldsymbol{\nabla} \cdot (-2\tilde{\eta}_W \boldsymbol{u}_W)\psi \, \mathrm{d}\boldsymbol{x}, \tag{4.15}$$

$${}^{\phi_{\text{GG}}}E^{\psi}_t = f \iint \boldsymbol{\nabla} \cdot (-2\tilde{\eta}_G \boldsymbol{u}_G)\psi \, \mathrm{d}\boldsymbol{x}, \tag{4.16}$$

$${}^{\phi_{\text{WG}}}E^{\psi}_t = f \iint \boldsymbol{\nabla} \cdot (-2\tilde{\eta}_G \boldsymbol{u}_W - 2\tilde{\eta}_W \boldsymbol{u}_G)\psi \, \mathrm{d}\boldsymbol{x}. \tag{4.17}$$

Figure 15 plots the time evolution of E^ψ for experiment T1 – just like 13a, but with ${}^{\phi}E^{\psi}_t$ broken up into three parts. Inspection of the figure shows that it is only ${}^{\phi_{\text{WW}}}E^{\psi}_t$ that balances out ${}^{WW}E^{\psi}_t$. We will add their analytical formulations together:

$${}^{WW}E^{\psi}_t + {}^{\phi_{\text{WW}}}E^{\psi}_t = \iint \boldsymbol{\nabla} \cdot (\zeta_W \boldsymbol{u}_W - 2\tilde{\eta}_W \boldsymbol{u}_W)\psi \, \mathrm{d}\boldsymbol{x} \tag{4.18}$$

$$= \iint \boldsymbol{\nabla} \cdot (\boldsymbol{u}_W[\zeta_W - 2\tilde{\eta}_W])\psi \, \mathrm{d}\boldsymbol{x} \tag{4.19}$$

$$= 0 \tag{4.20}$$

where we made use of the fact that waves contain no PV so that $\zeta_W = 2f\tilde{\eta}_W$. Therefore, quadratic wave terms have no net impact on E^ψ. However, we will see they have an indirect effect through the excitation of high-frequency baroclinic geostrophic currents.

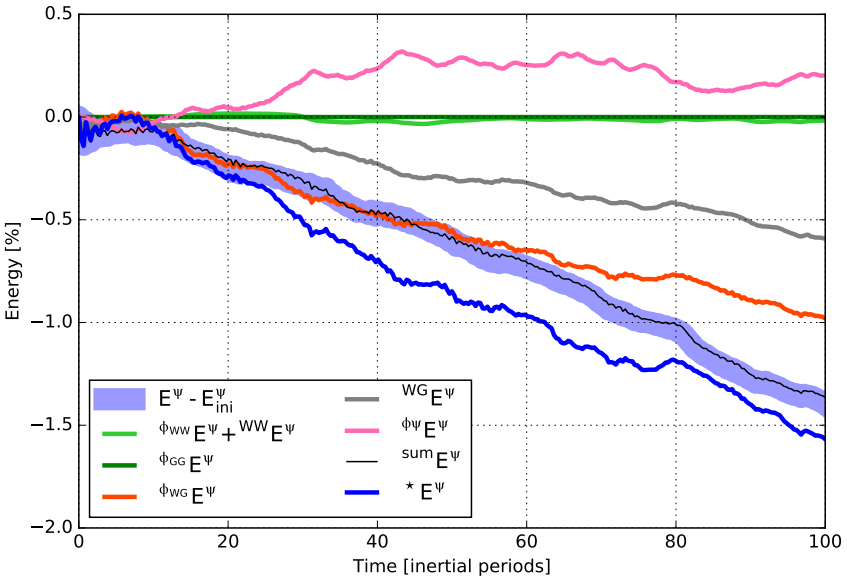

Figure 15: Experiment T1. E^{ψ} time series, reconstructed with the energy-evolution equations for each mode.

Figure 15 also reveals that ${}^{\phi_{GG}}E_t^{\psi}$ has a negligible amplitude. It is therefore ${}^{\phi_{WG}}E_t^{\psi}$ that mostly contributes to the transfer of energy, together with ${}^{WG}E^{\psi}$. We will add them together, and call the sum ${}^{\star}E_t^{\psi}$, getting:

$$
\begin{aligned}
{}^{\star}E_t^{\psi} &= {}^{WG}E_t^{\psi} + {}^{\phi_{WG}}E_t^{\psi} && (4.21)\\
&= \iint \boldsymbol{\nabla}\cdot(\zeta_G \boldsymbol{u}_W + \zeta_W \boldsymbol{u}_G - 2f\tilde{\eta}_G \boldsymbol{u}_W - 2f\tilde{\eta}_W \boldsymbol{u}_G)\,\psi\,\mathrm{d}\boldsymbol{x} && (4.22)\\
&= \iint \boldsymbol{\nabla}\cdot(\boldsymbol{u}_W[\zeta_G - 2f\tilde{\eta}_G] + \boldsymbol{u}_G[\zeta_W - 2f\tilde{\eta}_W])\,\psi\,\mathrm{d}\boldsymbol{x} && (4.23)\\
&= \iint \boldsymbol{\nabla}\cdot(\boldsymbol{u}_W[q_G] + \boldsymbol{u}_G[0])\,\psi\,\mathrm{d}\boldsymbol{x} && (4.24)\\
&= \iint \boldsymbol{\nabla}\cdot(q_G \boldsymbol{u}_W)\psi\,\mathrm{d}\boldsymbol{x}. && (4.25)
\end{aligned}
$$

Figure 15 shows how ${}^{\star}E^{\psi}$ (blue curve) gives a good estimate for the energy transfer $E^{\psi} - E^{\psi}_{\mathrm{ini}}$. Another graph where ${}^{\star}E^{\psi}$ is computed with $q = \zeta - 2f\tilde{\eta}$ (not shown) leads to the same conclusion.

Therefore, the baroclinic geostrophic mode, through q_G, has a very important role in the energy transfer from the balanced mode to the waves. Recall that there is basically no baroclinic geostrophic energy, i.e. mode G is almost zero. These very weak baroclinic geostrophic currents are nonetheless essential to generate the energy transfer from the balanced flow to the waves. The small amplitude of $\boldsymbol{u}_G$ also makes clear that the energy transfer is a second order effect. It is high-frequency and small-amplitude energy exchanges between waves and baroclinic geostrophic currents that allows q_G to contribute to the transfer $E^{\psi} \rightarrow E^{W}_{\mathrm{pot}}$.

In all experiments presented in this thesis, E^{ψ} systematically goes down. From looking at

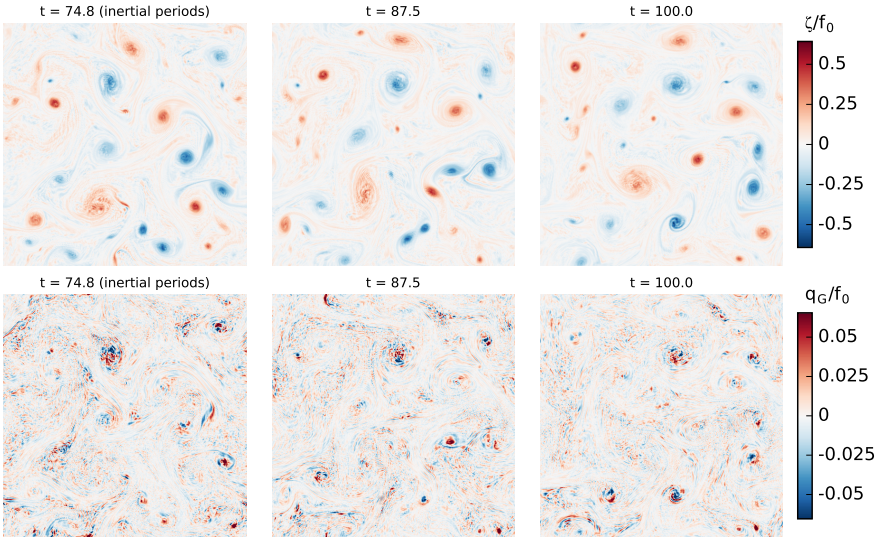

Figure 16: Experiment T1. Time evolution of ζ and q_G, late in the simulation. In the bottom panels, values of q_G/f_0 larger than 0.06 (smaller than -0.06) are shown in red (blue). x- and y-axes correspond to the zonal and meridional directions, spanning 1500 km $\times$ 1500 km.

(4.25), it is not obvious why. We can propose a dynamical explanation for this phenomenon. Recall that NIWs are concentrated in anti-cyclonic regions and expelled from cyclonic regions (c.f. section 1.3). Therefore, where ψ is positive (anti-cyclone), the divergence of $\boldsymbol{u}_W$ would be negative. If we assume q_G is positively correlated with $\boldsymbol{\nabla} \cdot \boldsymbol{u}_W$, the total product would yield a negative ${}^\star E_t^\psi$. It is not such a bad idea to think that q_G might be correlated with $\boldsymbol{\nabla} \cdot \boldsymbol{u}_W$; recall that q_G is generated by fast energy exchanges between modes G and W. Therefore, the baroclinic PV would allow waves to extract energy form the barotropic flow. While waves change their shape as they are concentrated to regions where the barotropic vorticity is negative, their scale reduces (because their initial scale is larger than the features in the background flow). This cascade stops when waves have the same length scale that the background flow, and so does the energy transfer.

Figure 16 plots ζ and q_G from experiment T1. As expected, q_G (bottom panels) concentrates in anti-cyclones (blue spots in top panels). Keeping in mind that the sign and shape of q_G changes quickly with time, we nonetheless have the impression that q_G is more positive in anti-cyclones, inspecting figure 16.

We still have not shown that it is the fast part of q_G that generates the energy transfer. According to the linear theory, the baroclinic geostrophic mode has only a slow-timescale evolution, but with the full nonlinear model, it also has "unbalanced", fast-timescale, components. Since q_G would be a "residual" of waves, we can imagine it would evolve on a fast timescale.

Before continuing, we will do a small aside on how fast (F) and slow (S) variables behave

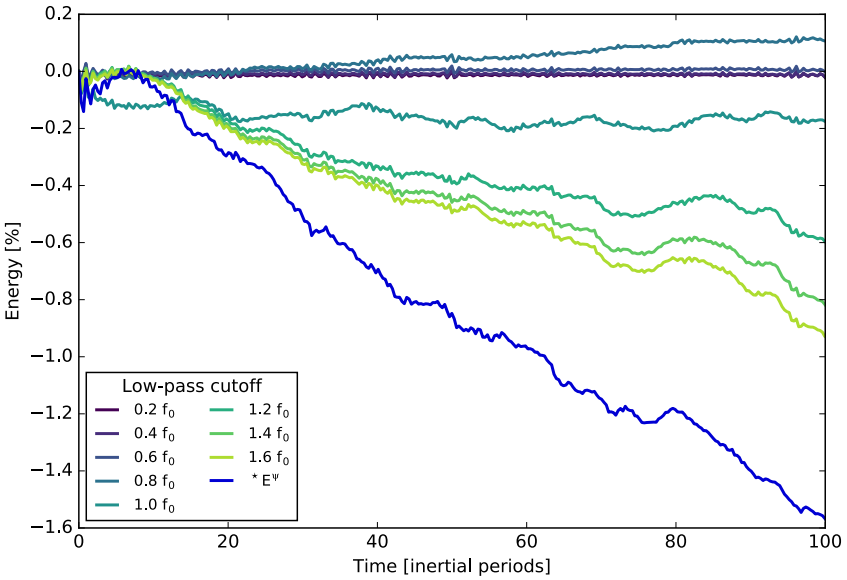

Figure 17: Experiment T1. Reconstruction of ${}^\star E^\psi$, with various low-pass time filters applied on q_G.

when subject to multiplication. Two fast variables multiplied together go like

$$\mathsf{FF} \sim \sin(\omega t)\sin(\omega t) \sim 1 + \cos(2\omega t) \sim \mathsf{S} + \mathsf{F}, \tag{4.26}$$

while a fast and a slow variable multiplied together give

$$\mathsf{FS} \sim \sin(\omega t) \times 1 \sim \sin(\omega t) \sim \mathsf{F}. \tag{4.27}$$

A net transfer of energy is considered as a slow product. Most terms in the energy-evolution equation for E^ψ are cubic, like ${}^\star E_t^\psi$. Therefore, a forcing on E^ψ can result from $\mathsf{FFS} \sim (\mathsf{S}+\mathsf{F})$ but not from $\mathsf{FSS} \sim \mathsf{F}$. Since $\boldsymbol{u}_W$ is fast and ψ is slow, we expect that q_G contains fast components.

To confirm this intuition, we applied low-pass time filters on q_G, before computing ${}^\star E_t^\psi$ again. Figure 17 presents the results. When only the slowest frequencies of q_G are kept, the transfer tends to zero. It becomes significant only when frequencies are kept up to a value of f_0, or faster. Therefore, it is the fast part of baroclinic geostrophic currents that contributes to the transfer between the barotropic flow and the waves.

4.3 Conclusion

In this thesis, some features of the interaction between NIWs and balanced flows were highlighted. Our framework, the two-layer shallow-water system, was complex enough to exhibit some interesting properties of the dynamics, and simple enough for us to understand mechanisms with compact expressions.

Our first conclusion is that our model was able to reproduce XV's results in some numerical experiments. XV's glm model averages fast inertial motions in order to only keep track of the

slow evolution of the flow, discarding wave phases. In an experiment where the background flow is particularly weak, our two-layer model fails to reproduce XV's results. We proposed an explanation for this disaccord,: when the interface deformation is not large enough, it does not allow the kinetic energy in the interface deformation field (E^C) to fill the increase in wave potential energy. Then, it is the wave kinetic energy that compensates for the increase in wave potential energy, breaking the wave action conservation.

We have been able to express, with a convenient expression, how the balanced flow loses energy to NIWs:

$$^{\star}E_t^{\psi} = \iint \boldsymbol{\nabla} \cdot (q_G \boldsymbol{u}_W)\psi \, \mathrm{d}\boldsymbol{x}. \tag{4.28}$$

In words, it means that the divergence of the flux of baroclinic PV by waves forces on the barotropic streamfunction. Recall that NIWs concentrate in anti-cyclones, i.e. where $\psi > 0$. At these locations, we can think that $\boldsymbol{\nabla} \cdot (q_G \boldsymbol{u}_W)$ is negative, meaning that $\boldsymbol{\nabla} \cdot (q_G \boldsymbol{u}_W)\psi$ would also be negative. Therefore, the integral would yield a negative value as waves are distorted by the background flow and energy would go from the balanced mode to waves.

To complete the current investigation, we suggest some avenues: i) Fix a problem in the two-layer model solver. Because the inverse Laplacian is computed in spectral space and the normal Laplacian is computed in Cartesian space, a small disparity is found between those two operations. Several robustness tests hint that this does not impact on results, but it is still an annoyance. ii) Compare our results with a two-layer Boussinesq model where the interface is fixed, but where buoyancy varies. We wonder if we would find the same energy transfer from the balanced flow to the waves in this different formalism. The barotropic divergent mode ϕ would be absent from the Boussinesq system, while it is very important in our model (recall how the strong forcing $^{WW}E_t^{\psi}$ is balanced out by $^{\phi_{\mathrm{WG}}}E_t^{\psi}$). On the other hand, the Boussinesq model would allow for surface buoyancy variance, which is absent in shallow water. iii) Run a forced-dissipative model where a baroclinically instable jet could exchange energy with waves, in analogy to the Antarctic Circumpolar Current. This set-up would give insight on a more realistic problem. iv) Perform a computation of $^{\star}E_t^{\psi}$ in a climatic model. This endeavor would demand great effort, but would probably give interesting results.

Bibliography

Matthew H Alford. Improved global maps and 54-year history of wind-work on ocean inertial motions. *Geophysical Research Letters*, 30(8), 2003.

Matthew H Alford, Jennifer A MacKinnon, Harper L Simmons, and Jonathan D Nash. Near-inertial internal gravity waves in the ocean. *Annual Review of Marine Science*, 8:95–123, 2016.

Eric Danioux, Jacques Vanneste, and Oliver Bühler. On the concentration of near-inertial waves in anticyclones. *Journal of Fluid Mechanics*, 773:R2, 2015.

Eric A D'Asaro, Charles C Eriksen, Murray D Levine, Clayton A Paulson, Peter Niiler, and Pim Van Meurs. Upper-ocean inertial currents forced by a strong storm. Part I: Data and comparisons with linear theory. 1995.

Aaron Gertz and David N Straub. Near-inertial oscillations and the damping of midlatitude gyres: A modeling study. *Journal of Physical Oceanography*, 39(9):2338–2350, 2009.

Adrian E Gill. *Atmosphere-Ocean Dynamics*, volume 30. Academic press, 1982.

Herbert Goldstein. *Classical Mechanics*. Pearson Education India, 1965.

Eric Kunze. Near-inertial wave propagation in geostrophic shear. *Journal of Physical Oceanography*, 15(5):544–565, 1985.

Eric Kunze and Thomas B Sanford. Observations of near-inertial waves in a front. *Journal of Physical Oceanography*, 14(3):566–581, 1984.

Kevin D Leaman and Thomas B Sanford. Vertical energy propagation of inertial waves: A vector spectral analysis of velocity profiles. *Journal of Geophysical Research*, 80(15), 1975.

Maxim Nikurashin and Raffaele Ferrari. Radiation and dissipation of internal waves generated by geostrophic motions impinging on small-scale topography: Application to the southern ocean. *Journal of Physical Oceanography*, 40(9):2025–2042, 2010.

Rick Salmon. *Lectures on Geophysical Fluid Dynamics*. Oxford University Press on Demand, 1998.

Henry M Stommel. *The Gulf Stream: A Physical and Dynamical Description*. Univ of California Press, 1958.

Stephanne Taylor and David Straub. Forced near-inertial motion and dissipation of low-frequency kinetic energy in a wind-driven channel flow. *Journal of Physical Oceanography*, 46(1):79–93, 2016.

Geoffrey K Vallis. *Atmospheric and Oceanic Fluid Dynamics: Fundamentals and Large-Scale Circulation*. Cambridge University Press, 2006.

J-H Xie and Jacques Vanneste. A generalised-lagrangian-mean model of the interactions between near-inertial waves and mean flow. *Journal of Fluid Mechanics*, 774:143–169, 2015.

WR Young and Mahdi Ben Jelloul. Propagation of near-inertial oscillations through a geostrophic flow. *Journal of Marine Research*, 55(4):735–766, 1997.

WR Young, Y-K Tsang, and NJ Balmforth. Near-inertial parametric subharmonic instability. *Journal of Fluid Mechanics*, 607:25–49, 2008.